Cooperative Capture Synthesis of Functionalized Heterorotaxanes: Chemical Scope, Kinetics, and Mechanistic Studies

d'Orchymont, Faustine ; Holland, Jason P

DOI: https://doi.org/10.1021/jacs.3c04111

JACS
JOURNAL OF THE AMERICAN CHEMICAL SOCIETY
pubs.acs.org/JACS
Article

Cooperative Capture Synthesis of Functionalized Heterorotaxanes—Chemical Scope, Kinetics, and Mechanistic Studies

Faustine d'Orchymont and Jason P. Holland*

Cite This: J. Am. Chem. Soc. 2023, 145, 12894−12910
Read Online
ACCESS | Metrics & More | Article Recommendations | Supporting Information

ABSTRACT: The self-assembly of molecularly interlocked molecules offers new opportunities for creating bioactive molecules for applications in medicine. Cooperative capture synthesis of heterorotaxanes in water is an attractive methodology for developing multifunctional supramolecular imaging agents or drugs, but derivatizing the rotaxane scaffold with biologically active vectors like peptides and proteins, or reporter probers like radioactive metal ion complexes and fluorophores, requires the installation of reactive functional groups. Here, we explored the chemical scope of β-cyclodextrin (β-CD) derivatization on the cucurbit[6]uril (CB[6])-mediated cooperative capture synthesis of hetero[4]rotaxanes with the objective of identifying which reactive groups can be used for further functionalization without compromising the efficiency of rotaxane synthesis. Nine β-CD derivatives featuring an electrophilic leaving group (tosylate), aliphatic amines, a carboxylic acid, aliphatic azides, anilines, and aryl isothiocyanate were evaluated in the synthesis of hetero[4]rotaxanes. Experimental measurements on the kinetics of rotaxane synthesis were combined with detailed computational studies using the density functional theory to elucidate the mechanistic pathways and rate determining step in the cooperative capture process. Computational studies on the structure and bonding also revealed why intermolecular interactions between the β-CD and CB[6] macrocycles improve the rate and efficiency of rotaxane formation through cooperative capture. Understanding the mechanistic details and synthetic scope will facilitate broader access to functionalized hetero[4]rotaxanes for applications in biomedicine and beyond.

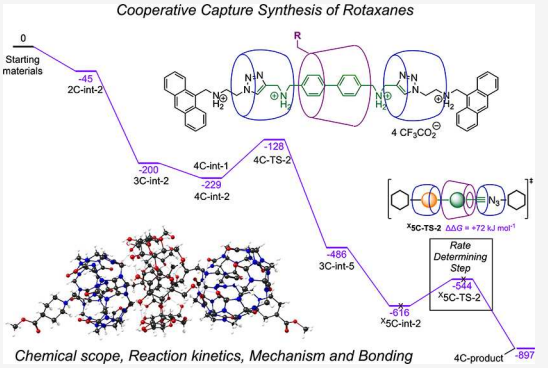

INTRODUCTION

Nature uses self-assembly to create a seemingly endless set of functional molecules that provide the framework for life.[1] Developing this level of complexity often involves combining matter in ways that use noncovalent interactions to synthesize compounds whose physical and biochemical properties extend beyond the sum of the individual components.[2,3] Supramolecular chemists strive to achieve the same complexity as nature, and over the last three decades, scientists have used the principles of self-assembly to produce artificial molecular machines,[4−7] molecular switches,[8] novel catalysts,[9,10] single molecule magnets,[11] and new materials for applications in biomedicine.[12−21]

Supramolecular compounds derived from molecular cages,[22−33] and from molecularly interlocked molecules like rotaxanes[34] and catenanes,[35−38] have shown promise in several applications[14,15] such as delivery vehicles[39−42] for controlling the release of cytotoxic drugs,[43−45] as biosensors for DNA recognition,[46,47] and as reporter probes for diagnostic molecular imaging.[48−57] Efficient synthesis of supramolecular compounds in water[58] is one of the main challenges that must be overcome to generate a wider pool of drugs for applications in biomedical imaging or therapy. In this regard, rotaxanes represent an excellent platform for accessing new types of biologically active supramolecular agents.[59−62]

Recently, we developed a rotaxane-based platform to create supramolecular radiotracers for targeted imaging of cancer biomarkers *in vivo*.[63,64] Our synthesis of functionalized rotaxanes uses self-assembly via a cooperative capture strategy.[65−68] This approach builds on the classic cucurbit[6]-uril[69,70] CB[6]-mediated alkyne-azide "click" reaction, first described by Mock et al. during the 1980s.[71−73] The chemistry was proven successful in the creation of both antibody- and peptide-based rotaxane radiotracers that target a multitude of cancer biomarkers including human epidermal growth-factor receptor 2 (HER2/*neu*) in ovarian cancer, human hepatocyte growth factor receptor (c-MET) in gastrointestinal cancer, and

Received: April 20, 2023
Published: June 5, 2023

Scheme 1. Synthesis of the Monofunctionalized β-CD-R Derivatives (3−11) Featuring Azide, Aliphatic Primary Amine, Carboxylic Acid, Aniline, and Benzyl-Isothiocyanate Groups as Reactive Handles[a]

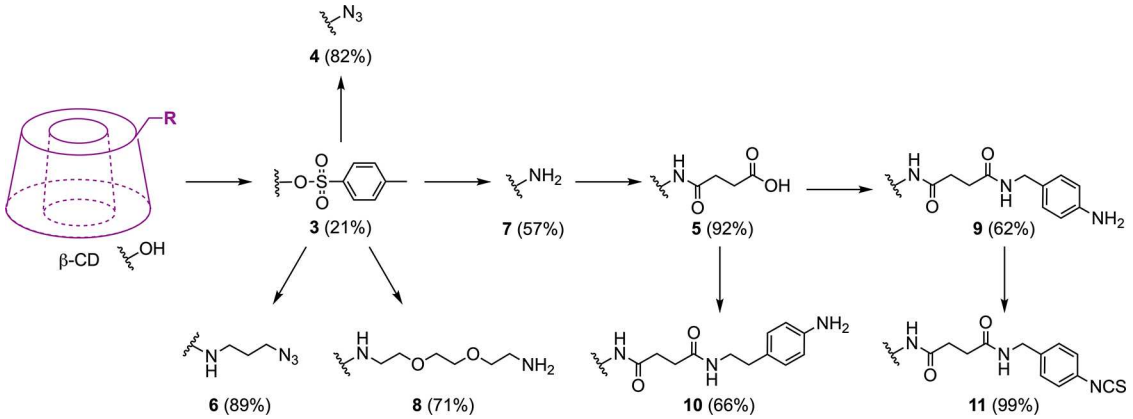

[a]Synthetic details and characterization data for compounds **3**, **4**, **5**, and **7** were reported elsewhere.[63] Data for compounds **6**, and **8**−**11**, are presented in supplemental Figures S1−S14.

prostate-specific membrane antigen (PSMA) in prostate cancer. Nevertheless, to expand the chemical scope and facilitate the synthesis of a more diverse portfolio of bioactive rotaxanes, it is important to understand the reactivity, mechanism, and chemical limitations of the cooperative capture strategy. Here, we used a model system to explore the influence of β-cyclodextrin (β-CD) macrocycle functionalization on rotaxane synthesis. Our objectives were to identify reactive functional groups that could be appended to β-CD to facilitate further derivatization with biologically active targeting vectors or imaging probes, without compromising rotaxane self-assembly. Experimental studies on the reaction kinetics were combined with extensive density functional theory (DFT) calculations to elucidate the mechanistic pathway and identify the rate determining step involved in the dual cooperative capture synthesis of hetero[4]rotaxanes. Further analysis of the intermolecular bonding interactions also shed light on the important role of CB[6] and β-CD in accelerating the rate and efficiency of triazole synthesis via the CB[6]-encapsulated alkyne-azide click reaction.

METHODS

Full details on the methods, materials, synthesis, and characterization of all compounds are presented in the Supporting Information. Experimental high-performance liquid chromatography (HPLC) chromatograms, high-resolution electrospray ionization mass spectrometry (HR-ESI-MS) data, 1-dimensional ^{1}H- and ^{13}C{^{1}H}-NMR spectra, 2-dimensional NMR analyses, and NMR titration data are presented in supplemental Schemes S1−S8, Figures S1−S135, and Tables S1−S8. Complete experimental and simulated data supporting the kinetic studies are presented in supplemental Figures S136−S139 and Tables S9−S20. Computational details and supporting data from the Natural Bond Orbital (NBO) analysis and additional details on the reaction coordinates are presented in supplemental Figures S140−S141 and Tables S21−S22. Cartesian coordinates of all DFT-optimized structures are also provided.

RESULTS AND DISCUSSION

Synthesis of Monofunctionalized β-CD Derivatives. Recently, we demonstrated that functionalization of the β-CD macrocycle is a convenient way of introducing either a biologically active vector to target cancer biomarkers or a multidentate *aza*-macrocyclic chelate for complexation of radioactive metal ions.[63] These pilot experiments relied on the derivatization of nonfunctionalized β-CD at one of the seven primary hydroxyl groups of the glucopyranose units with, for example, a photochemically active aryl azide group (ArN_3). Although the photochemical bioconjugation approach allowed us to synthesize viable ^{68}Ga- and ^{89}Zr-rotaxane-based radiotracers for applications in positron emission tomography (PET) imaging *in vivo*, introducing alternative reactive handles would increase the chemical scope and versatility of functionalized rotaxane formation through cooperative capture synthesis.

The presence of 7 primary and 14 secondary hydroxyl groups makes selective modifications of β-CD extremely challenging.[74] However, minor differences in the reactivity of the hydroxyl groups have been exploited to allow for β-CD functionalization with high selectivity and purity.[75] Notably, the primary hydroxyl groups in the 6-position are the most nucleophilic, the secondary hydroxyl groups in the 2-position are the most acidic ($pK_a \sim 12.1$), and the secondary hydroxyl groups in the 3-position are the least accessible and also the least reactive.[76−78] Functionalization of the secondary face of β-CD typically requires the use of protecting groups, whereas methods for reacting one of the primary hydroxyl group are well-established.[79−81] The ability of cyclodextrins to act as host macrocycles and form molecular inclusion complexes has also been exploited to direct the synthesis of functionalized β-CD compounds, where selective derivatization on one face can be achieved depending on the orientation of the reagent inside the cavity.[82−84] Recent advanced methods have also reported the site-selective hetero- and poly-functionalization of α-CD[85] and β-CD[86] by using a series of innovative tandem, azide, or thioether reduction/diisobutylaluminum hydride (DIBAL-H) promoted debenzylation strategies. Considering these synthetic precedents, and with the objective of retaining control over the stoichiometry, chemical properties, and regioisomerism, we focused on evaluating the chemical scope of β-CD-R derivatives functionalized at one of the primary hydroxyl positions in the synthesis of hetero[4]rotaxanes. A series of monofunctionalized β-CD-R derivatives featuring reactive groups that can be used in further conjugation steps were synthesized (compounds **3**−**11**, Scheme 1). The β-CD-R macrocycles included species with azides (**4** and **6**), primary amines (**7** and **8**), carboxylic acid (**5**), aryl amines (**9** and **10**), and aryl isothiocyanate (**11**) groups. The mono-6-deoxy-6-(4-

https://doi.org/10.1021/jacs.3c04111
J. Am. Chem. Soc. 2023, 145, 12894−12910

Scheme 2. General Reaction Pathway and Reagent Scope for the Reversible Molecular Inclusion of Biphenyl-Dialkyne (1) Inside the β-CD Cavity and Subsequent CB[6]-Mediated Azide-Alkyne Click Reactions to Form [4]Rotaxanes[a]

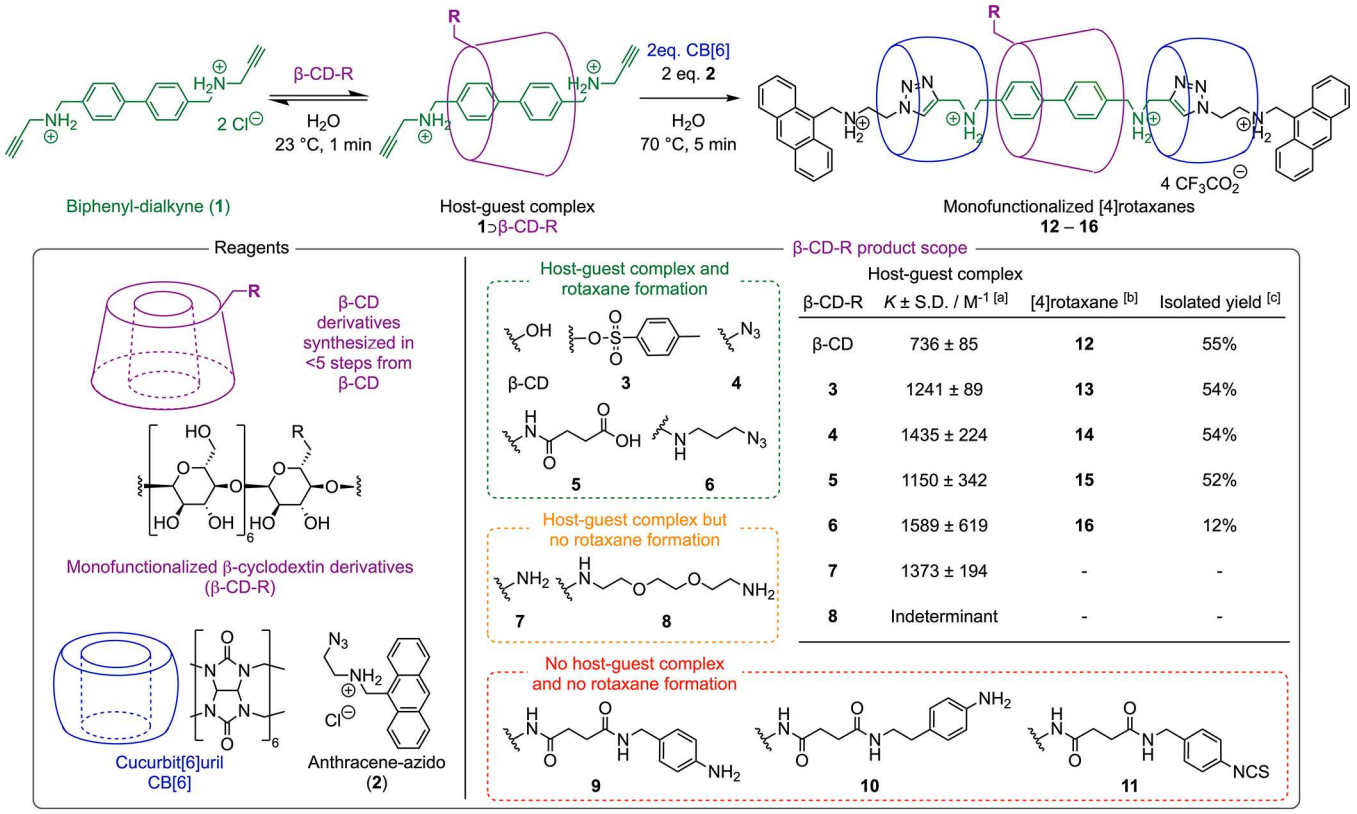

Host-guest complex β-CD-R	K ± S.D. / M^{-1} [a]	[4]rotaxane [b]	Isolated yield [c]
β-CD	736 ± 85	**12**	55%
3	1241 ± 89	**13**	54%
4	1435 ± 224	**14**	54%
5	1150 ± 342	**15**	52%
6	1589 ± 619	**16**	12%
7	1373 ± 194	-	-
8	Indeterminant	-	-

[a] Binding constants are expressed as the mean (M^{-1}) ± one standard deviation (S.D. / M^{-1}) from n = 3–6 independent measurements.
[b] Reactions were conducted with: β-CD-R (1.7 μmol, 1 eq.), compound **1** (1.7 μmol, 1 eq.), CB[6] (3.4 μmol, 2 eq.), and compound **2** (3.4 μmol, 2 eq.), in H_2O (0.5 mL) at 70 °C for 5 min.
[c] Isolated yield after semipreparative HPLC purification.

[a]The β-CD-R derivatives (β-CD, and compound **3**–**6**, green box) lead to [4]rotaxane (compounds **12**–**16**) formation, derivatives **7** and **8** (yellow box) form host-guest complexes with **1** but do not generate the equivalent [4]rotaxane species, and reagents **9**–**11** (red box) do not form molecular inclusion complexes with **1** or the corresponding [4]rotaxanes.

tosyl)-β-CD (monotosyl β-CD, **3**)[87−95] is the key intermediate required in the synthesis of the various β-CD-R derivatives, which can be accessed via nucleophilic substitution of the tosyl group, and through subsequent standard chemical transformations. The relatively low yield of the reaction to obtain **3** (21%) can be explained by the formation of randomly substituted products, typically with substitution of β-CD >1. Nevertheless, compound **3** can be isolated in gram quantities[63] and in high chemical purity from commercially available starting materials. From compound **3**, the other functionalized β-CD-R derivatives (**4**−**11**) can be accessed in 1-to-4 linear steps in good-to-high yields (Scheme 1, and supplemental Scheme S1 and Figures S1−S14).

Chemical Scope of Molecular Inclusion and [4]-Rotaxane Synthesis Using β-CD Derivatives. An overview showing the general reaction for the synthesis of [4]rotaxanes from a mixture containing the biphenyl-dialkyne guest molecule **1**, the β-CD derivative (β-CD-R; compounds **3**−**11**), CB[6], and the anthracene-azido compound **2** in a 1:1:2:2 stoichiometric ratio is presented in Scheme 2. In the complete (full) reaction pathway, an initial molecular inclusion complex (**1** ⊃ β-CD-R) forms between the biphenyl-dialkyne guest molecule **1** and β-CD-R derivative. Further details on the experimental measurements of the molecular inclusion between guest molecule **1** and β-CD-R derivatives **3**−**11** using ^{1}H-NMR titrations are presented in supplemental Figures S15−S21 and Tables S1−S7. Then, the [4]rotaxane synthesis proceeds via a double CB[6]-accelerated click reaction between the anthracene-azido **2** and alkyne groups of guest molecule **1**, thereby capping both ends of the axle with anthracene stoppers and trapping the three macrocyclic rings noncovalently. Formation of the **1** ⊃ β-CD molecular inclusion complex is a prerequisite for [4]rotaxane synthesis and is expected to occur rapidly and reversibly at room temperature, with the position of equilibrium favoring the complex formation.[63] The second part of the reaction pathway, involving a double CB[6]-accelerated click process, is likely to occur in a stepwise fashion (see the kinetic and computational sections below) with successful [4]rotaxane synthesis observed in <5 min when the reaction mixtures were heated to 70 °C. Importantly, and despite solubility issues with CB[6] (*vide infra*), the reaction generally proceeds smoothly in water. For example, in our baseline (positive control) reaction using unsubstituted β-CD, ^{1}H-NMR titrations with **1** confirmed the formation of the **1** ⊃ β-CD inclusion complex with a 1:1 stoichiometric ratio between the two components. The chemical shifts observed for resonance peaks associated with aromatic protons H_a and H_b of the guest molecule **1** (see

https://doi.org/10.1021/jacs.3c04111
J. Am. Chem. Soc. 2023, 145, 12894−12910

Scheme 3. Control Reaction Showing the Formation of the [2]Semirotaxane Intermediate 28 and Homo[3]rotaxane 29 Starting from a 1:2:2 Stoichiometric Ratio of Biphenyl-dialkyne 1, CB[6], and the Anthracene-azido Stopper 2

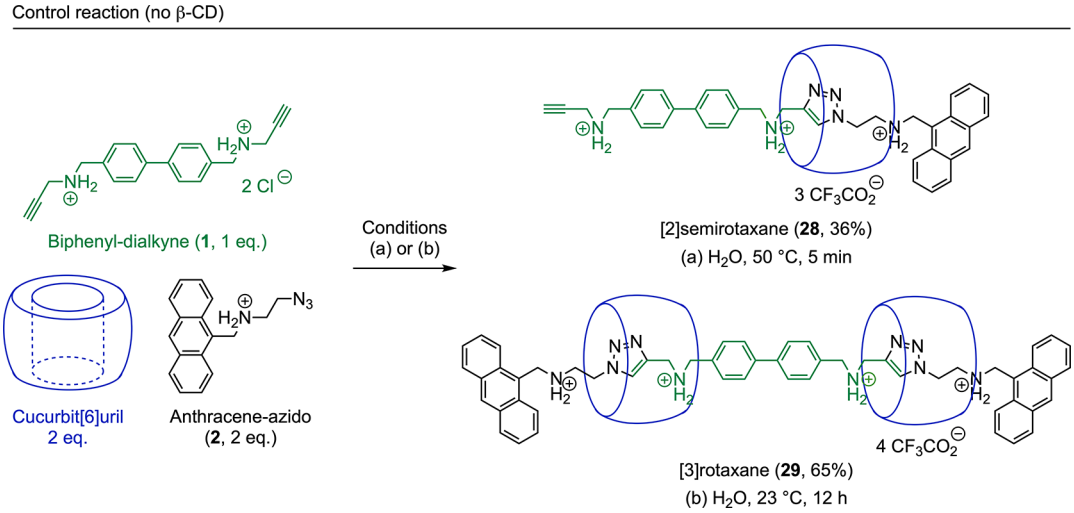

supplemental Figure S16 for structure assignments) confirmed the dynamic process of the complexation, with **1** being in a fast exchange between the free and bound states (relative to the NMR timescale). Analysis of the experimental ^{1}H-NMR chemical shift data by using three different binding models: the Benesi-Hildebrand,[96] Scott[97] and Scatchard[98] models, gave an overall average association constant of K_a = 736 ± 85 M^{-1}, computed as the mean ± one standard deviation (supplemental Figure S16 and Table S2).

^{1}H-NMR titration experiments confirmed the formation of **1** ⊃ *β*-CD-R inclusion complexes with 1:1 stoichiometry when using derivatives **3**−**8** (supplemental Figures S15−S21 and Tables S1−S7). For *β*-CD-R derivatives **3**−**7**, the calculated average association constants were between 1150 ± 342 M^{-1} (compound **5**) and 1589 ± 619 M^{-1} (compound **6**). In each case, these values were significantly higher than the association constant observed for the **1** ⊃ *β*-CD inclusion complex using unsubstituted *β*-CD, suggesting that, in some cases, additional stabilizing interactions may occur between the reactive handle and biphenyl-dialkyne guest **1**, which, in the fully protonated form, contains 4 hydrogen bond donors. Experimental evidence for the formation of the molecular inclusion complex **1** ⊃ **8** was also observed from ^{1}H-NMR titrations, but the chemical shift data were insufficient to determine the association constant with the required accuracy. For *β*-CD-R derivatives **9**−**11**, which feature *para*-substituted arene rings as reactive handles for bioconjugation, no evidence of host-guest complex formation with **1** was observed.

After evaluating the host-guest complexation between **1** and *β*-CD-R derivatives **3**−**11**, we next attempted the synthesis of the corresponding [4]rotaxane species via reaction with 2 equivalents of both CB[6] and the anthracene-azido compound **2** in H_2O at 70 °C for 5 min (Scheme 2). The anthracene-azido stopper (**2**) was synthesized with an overall yield of 35% after three steps starting from commercially available 9-anthracenecarboxaldehyde by using methods adapted from Jenie et al. (supplemental Scheme S2 and Figures S22−S26).[99] For reactions that successfully yielded the desired [4]rotaxanes **12**−**16**, details on the synthesis and characterization by using high-performance liquid chromatography (HPLC), high-resolution electrospray ionization mass spectrometry (HRMS), and a combination of both 1-dimensional and 2-dimensional ^{1}H- and ^{13}C{^{1}H}-NMR spectroscopy are presented in supplemental Scheme S3, and Figures S27−S51. The [4]rotaxanes **12**−**15** were isolated after purification by using preparative HPLC with yields from 52 to 55%. The [4]rotaxane **16** formed by reaction with the alkyl-azide *β*-CD derivative **6** was isolated with a low yield of only 12%. Importantly, isolation of compounds **12**−**16** confirmed that the cooperative capture strategy can be adapted to access hetero[4]rotaxane species that present an electrophile (tosyl-derivative **13**), a carboxylic acid (compound **15**), and aliphatic azides (compounds **14** and **16**) as simple reaction handles for use in further conjugation steps with biologically active vectors such as peptides, antibodies, or drug molecules. This observation increases the chemical scope for constructing bioactive supramolecular agents via nucleophilic substitution, amide bond formation, or bioorthogonal azide-alkyne click reactions. In contrast, no rotaxane formation was observed when using the *β*-CD derivatives **7**−**11**. The lack of host-guest complex formation is likely to be the reason why compounds **9**−**11** failed to produce the corresponding [4]rotaxanes. In the case of compounds **7** and **8**, where molecular inclusion of **1** was observed, we postulate that the inability of these *β*-CD derivatives to form the corresponding [4]rotaxane species in our test reaction is potentially due to self-inclusion of the reactive tether[100] inside the *β*-CD cavity or steric hindrance, which may inhibit stabilizing interactions between the substituted primary face of the *β*-CD-R derivative and the CB[6].

In addition to the synthesis of rotaxanes featuring anthracene stoppers on the axle termini, we also investigated the use of peptide-based stoppers (compounds **17**−**22**, supplemental Schemes S4−S5, Figures S52−S72). Changing the nature of the stopper did not impinge on the success of the rotaxane formation. For the *β*-CD-azide derivatives **4** and **6**, we also investigated the use of classic copper ion-mediated azide-alkyne click or strain-promoted click reactions to create more elaborate *β*-CD derivates featuring metal ion binding chelates (compounds **23**−**27**, supplemental Schemes S6−S7, Figures S73−S123).

Collectively, our synthetic data demonstrate that a range of monofunctionalized *β*-CD derivatives can be successfully used to design and synthesize more elaborate hetero[4]rotaxanes for

https://doi.org/10.1021/jacs.3c04111
J. Am. Chem. Soc. 2023, 145, 12894−12910

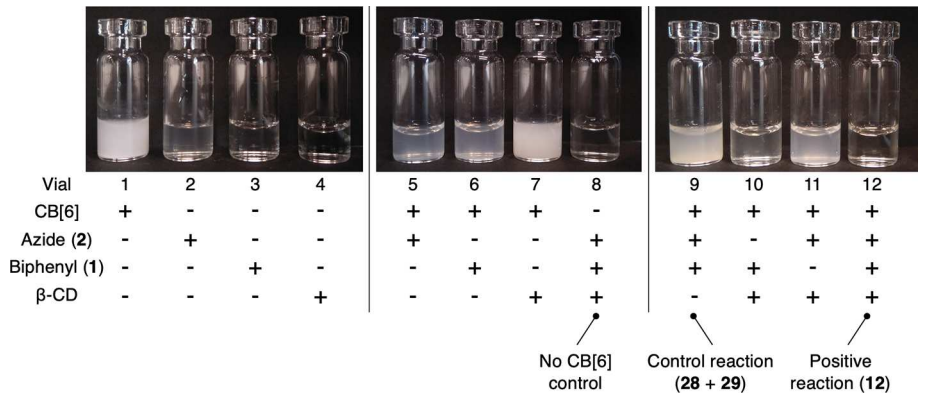

Figure 1. Photographs showing the change in solution opacity upon dissolution of CB[6] in water at 23 °C in the presence of the different reaction components: β-CD, anthracene-azido compound **2**, and biphenyl compound **1**. Note: in all reactions, the volume was constant (0.5 mL), and in each case, a fixed amount of different components was added (m(CB[6]) = 2.19 mg, m(anthracene-azido **2**) = 0.69 mg, m(biphenyl-dialkyne **1**) = 0.32 mg, m(β-CD) = 1.25 mg) corresponding to a 2:2:1:1 stoichiometry of CB[6]:**2**:**1**:β-CD in the positive reaction forming [4]rotaxane **12**. Vial 9 corresponds to the control reaction without β-CD, and vial 12 shows the full (positive) reaction leading to the synthesis of [4]rotaxane **12**.

potential applications in biomedicine. However, careful consideration must be paid to the nature of the reactive handle, and choice of subsequent coupling chemistry, and on the potential effects of appending acyclic ligands to the β-CD unit on both the molecular inclusion and cooperative capture steps of the rotaxane synthesis.

Rotaxane Synthesis in the Absence of β-CD. The CB[6]-catalyzed azide-alkyne click reaction was originally developed without using β-CD as an additive.[71−73] Stoddart and co-workers later demonstrated that adding one equivalent of a second macrocycle as a cofactor, such as β-CD,[65,66] pillar[5]arene,[67] or pillar[6]arenes,[68] greatly improved the efficiency of the hetero[4]rotaxane synthesis. Mechanistically, it has been hypothesized that the presence of the second ring helps to rigidify the CB[6] macrocycles, which enhances the rate of triazole synthesis and increases the propensity toward rotaxane formation.[66] Before investigating the kinetics and mechanism of the cooperative capture synthesis of hetero[4]-rotaxanes, it was necessary to synthesize two key byproducts that can form in the absence of the β-CD cofactor. The reaction of one equivalent of biphenyl-dialkyne **1** with 2 equivalents of both CB[6] and the anthracene-azido stopper **2** to form both the [2]semirotaxane intermediate **28** and the homo[3]rotaxane **29** is depicted in Scheme 3. Characterization data for compounds **28** and **29** are presented in supplemental Scheme S8 and Figures S124−S134.

It is important to note that the synthesis and isolation of [2]semirotaxane **28** and [3]rotaxane **29** in water required different conditions from those used for the full reaction involving β-CD (Scheme 2). Elevated temperatures increased the conversion to the [2]semirotaxane **28**, which was isolated in 36% yield, but prolonged heating led to decomposition of this key intermediate, likely via dethreading of the CB[6] macrocycle from the axle.[63] Successful synthesis of [3]rotaxane **29** in 65% yield required a longer reaction performed at room temperature for 12 h. This observation is consistent with previous reports in which β-CD (or indeed pillar[5 or 6]arene macrocycles) were found to increase the rate of rotaxane formation via cooperative capture.[65−68]

Dissolution of CB[6] during Rotaxane Synthesis. One of the limiting factors in the rate of synthesis of the [2]semirotaxane **28** and homo[3]rotaxane **29** was found to be the dissolution of CB[6] under the given reaction conditions and using water as a solvent. Since dissolution was crucial to the design of our kinetic experiments (*vide infra*), we investigated this process in detail. To illustrate, Figure 1 shows a photograph of 12 separate reaction vials containing different permutations of the four reaction components required for the synthesis of compounds **28**, **29**, or the full hetero[4]rotaxane **12**. Reagents were mixed in 0.5 mL of water at a fixed concentration and in the appropriate stoichiometric ratio that would, in the case of the positive reaction, lead to the synthesis of [4]rotaxane **12**. The biphenyl-dialkyne **1**, anthracene-azido **2**, and β-CD are completely soluble (vials 2−4, respectively), whereas CB[6] alone (vial 1) produced a milky white suspension. Mixing CB[6] with either compound **1** or **2** (vials 5 and 6) reduced the solution opacity through improved CB[6] solubility, but the addition of β-CD to the suspension of CB[6] had no effect (vial 7). In the absence of CB[6], the mixture of **1**, **2**, and β-CD remains clear and colorless (vial 8) with only starting materials present and no triazole products identified. Interestingly, mixing CB[6] with both **1** and **2** (vial 9), as in the control reaction used for the synthesis of **28** and **29**, showed only a marginal decrease in solution opacity. This observation is consistent with our synthetic work in which prolonged reaction times were required to isolate [3]rotaxane **29** (*vide supra*). Mixing CB[6] with β-CD and either compound **1** (vial 10) or **2** (vial 11) showed clear improvements in the solubility of CB[6] and suggested that, in both cases, the reversible formation of ternary inclusion complexes involving all three components is likely to occur in solution. Finally, for the positive reaction containing all four reaction components (vial 12: CB[6]:**2**:**1**:β-CD in a stoichiometric ratio of 2:2:1:1), a completely clear and colorless solution was produced. Earlier characterization of this reaction mixture using HPLC, HRMS, and multinuclear NMR spectroscopy confirmed that only the full hetero[3]rotaxane **12** was present and no formation of the other possible byproducts **28** or **29** was observed. These data provided valuable information from which we were able to select and standardize the appropriate reaction conditions used when performing the kinetic studies.

Kinetic Studies on Rotaxane Synthesis via Cooperative Capture. Prior to measuring the kinetics of rotaxane conversion in solution, it was important to establish a reliable method for separating and quantifying the various species

https://doi.org/10.1021/jacs.3c04111
J. Am. Chem. Soc. 2023, 145, 12894−12910

present in both the full reaction forming [4]rotaxane **12** (via the intermediate molecular inclusion complex **28** ⊃ β-CD) and in the control reaction without β-CD leading to the byproducts [2]semirotaxane **28** and homo[3]rotaxane **29**. We adjusted the concentrations to ensure that the reaction would run to near completion within a 30 min experimental window and that aliquots could be withdraw at specified time points for immediate analysis by using reverse-phase HPLC. HPLC chromatograms from the aliquots recorded over time by using electronic absorption at 280 nm are presented in Figure 2 and

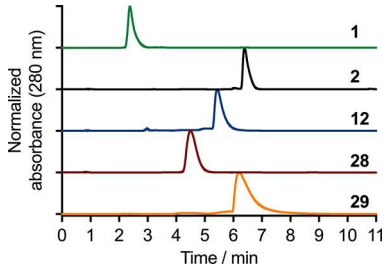

Figure 2. Reverse-phase analytical HPLC chromatograms showing the separation of the starting materials **1** and **2**, the desired [4]rotaxane product **12** obtained from the full reaction including β-CD, and the [2]semirotaxane intermediate **28** and homo[3]rotaxane byproduct **29** obtained from the control reaction without β-CD. HPLC chromatograms were measured at 280 nm and obtained by using a flow rate of 0.7 mL min^{-1} and a linear gradient of A (methanol, Sigma-Aldrich, HPLC grade) and B (distilled water containing 0.1% trifluoroacetic acid [TFA]): t = 0 min A 50% + B 50%, t = 10 min A 100% + B 0%.

show the retention times and clear separation of the various reaction components (compounds **1**, **2**, **12**, **28**, and **29**). Careful calibration experiments were performed to account for the differences in molar absorption of the various species at 280 nm (supplemental Figure S136) and allow accurate quantification of the relative mole fraction of each species after normalization of the chromatograms. Normalization was important because fluctuations in the injection volume delivered onto the HPLC column using our automated machine meant that absolute quantification was not possible. Notably, CB[6] and β-CD do not absorb at 280 nm and their change in concentrations could not be followed directly. In addition, compound **2** was not followed during the kinetic studies because this species has a very weak chromophore at 280 nm, which generates only a low-intensity signal below ∼3 mM concentration that was in the noise range of the detector (absorbance <0.1 at 280 nm, supplemental Figure S136, panels B and F). Compound **2** also displayed a retention time that overlapped with the byproduct homo[3]rotaxane **29**. However, at the concentrations used in the kinetic studies, quantification of compound **29** in the control reaction was only marginally influenced by the change in concentration of compound **2**.

To follow the kinetics of the full reaction leading to [4]rotaxane **12**, CB[6] (2.30 mg, 2.3 μmol, 4.62 mM, 2.1 equiv) was added to a solution containing β-CD (1.37 mg, 1.2 μmol, 2.41 mM, 1.09 equiv), compound **1** (0.32 mg, 1.1 μmol, 2.20 mM, 1 equiv), and compound **2** (0.73 mg, 2.3 μmol, 4.66 mM, 2.1 equiv) in H_2O (0.5 mL). The resulting mixtures were heated at the specified temperatures (70, 50, 35, or 23 °C) for 30 min. No reaction occurs without CB[6] (supplemental Figure S139, panel I), and therefore, this regent was added last. Compound **1** was selected as the limiting reagent, with the other reagents present in a slight excess to ensure that an accurate amount of highly absorbing biphenyl species was delivered in each experiment and that the total signal intensity of HPLC chromatograms was in the same range across all samples. A total of 15 aliquots (5 μL/each) were withdrawn from the reaction mixtures, with 1 min sampling intervals in the first 10 min, followed by sampling every 5 min until the reactions were essentially complete by 30 min. Where feasible, experiments were performed in triplicate by using independent replicates. For the control reaction, the experimental conditions and starting concentrations of CB[6], **1**, and **2** were the same as used in the full reaction, but β-CD was not added to the mixture. Experimental data obtained for the full reaction run at 50 °C are presented in Figure 3 where panel A shows the evolution in peak intensities over time as stack plot of the HPLC chromatograms recorded during the experiment. Complete experimental data on the measured change in mole fractions as well as the optimized kinetic simulation curves are given in supplemental Tables S9−S20. Additional kinetic plots are presented in supplemental Figures S137−S139.

After correcting the measured peak areas from the HPLC for the various identifiable species by using our calibration curves (supplemental Figure S136), data were normalized and converted into the measured change in mole fraction *versus* time (Figure 3, panel B). The simplest mechanistic pathway for the full reaction to give [4]rotaxane **12**, and which produced the best kinetic simulations of the experimental data using a global fitting algorithm, is presented in Scheme 4. In the case of the full reaction, rapid equilibrium for the host-guest complex formation between **1** and β-CD (as observed from the earlier ^{1}H-NMR titration experiments, *vide supra*) means that the signal observed (Figure 3, panels A and B, green peaks and green square data points) is a composite of both unbound **1** and the molecular inclusion complex **1** ⊃ β-CD. Due to rapid dissociation of the **1** ⊃ β-CD inclusion complex under the HPLC conditions, it is not possible to separate these two components. A similar situation occurs for the key intermediate species **28**, which can also be present in solution as the molecular inclusion complex **28** ⊃ β-CD (Figure 3, panels A and B, red peaks and red diamond data points). The data observed for [4]rotaxane **12** correspond to the unique product (Figure 3, panels A and B, blue peaks and blue circle data points). As can be seen in the experimental data, the reaction proceeds rapidly with almost complete conversion of the starting material **1** after 10 min. Initially, a rapid increase in the concentration of the intermediate species (**28** and **28** ⊃ β-CD) was observed. It is important to note that the synthesis of [4]rotaxane **12** requires the formation of **28** ⊃ β-CD. Since the [3]rotaxane **29** byproduct is not observed in this reaction, we can conclude that the position of equilibrium between the [2]semirotaxane **28** and[3]semirotaxane **28** ⊃ β-CD lies toward the β-CD bound species. To confirm that, (i) the molecular inclusion complex **28** ⊃ β-CD is formed, and (ii) that the position of equilibrium lies heavily toward the side of the inclusion complex, ^{1}H-NMR titrations were performed (supplemental Figure S135 and Table S8). The average association constant between **28** and β-CD to form the molecular inclusion complex **28** ⊃ β-CD found to be K_a = 18,067 ± 7573 M^{-1}. After an initial peak at a mole fraction of 0.58 at approximately 3 min, the concentrations of **28** and **28** ⊃ β-CD decrease slowly and [4]rotaxane **12** forms over a longer time. This observation indicates that a stepwise reaction occurs in which the second step is rate limiting.

https://doi.org/10.1021/jacs.3c04111
J. Am. Chem. Soc. 2023, 145, 12894−12910

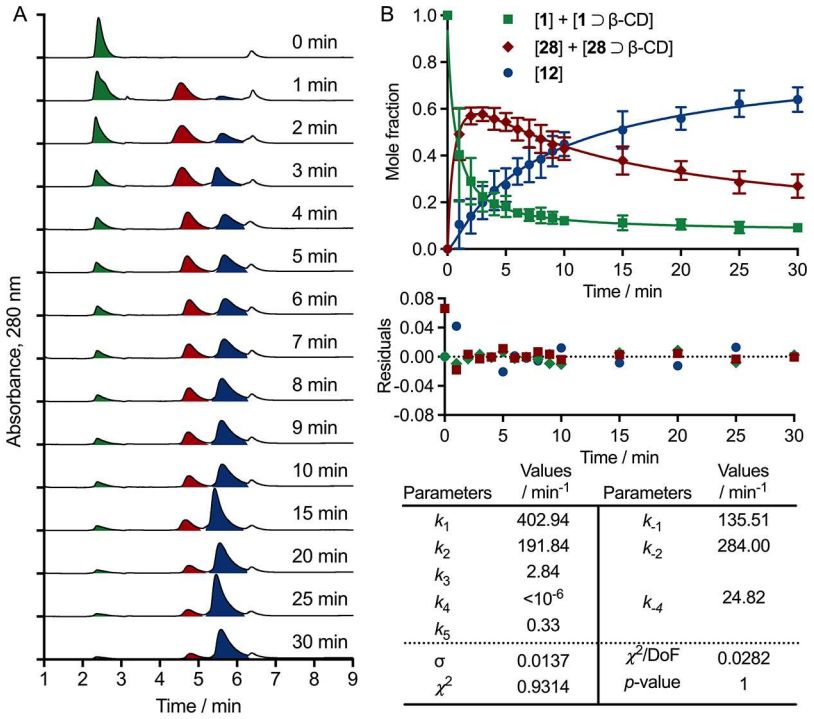

Parameters	Values / min^{-1}	Parameters	Values / min^{-1}
k_1	402.94	k_{-1}	135.51
k_2	191.84	k_{-2}	284.00
k_3	2.84		
k_4	$<10^{-6}$	k_{-4}	24.82
k_5	0.33		
σ	0.0137	χ^2/DoF	0.0282
χ^2	0.9314	*p*-value	1

Figure 3. Experimental data and kinetic simulation of the full reaction pathway leading to the synthesis of [4]rotaxane **12**. (A) Stack plot showing the evolution of the HPLC profile of the reaction mixture over time for the synthesis of [4]rotaxane **12** in H_2O at 50 °C. With reference to the reaction pathway shown in Scheme 4, the peaks highlighted refer to the summation of **1** and the molecular inclusion complex **1** ⊃ *β*-CD (green), the key intermediate species **28** and **28** ⊃ *β*-CD (red), and the final product [4]rotaxane **12** (blue). (B) Plot of the experimentally measured mole fractions for the starting materials (**1** + **1** ⊃ *β*-CD, green squares), intermediates (**28** + **28** ⊃ *β*-CD, red diamonds), and product (**12**, blue circles). Data points and error bars indicate the mean ± 1 standard deviation measured from independent triplicate experiments (n = 3). Solid lines show the optimum fit of the experimental data obtained by using the kinetic model shown in Scheme 4 with simulations calculated by using *KinTek Global Kinetic Explorer* (version v11.0.1, KinTek Corporation, Snow Shoe, PA, United States of America).

Kinetic simulations using the mechanistic pathway represented in Scheme 4 allowed us to model the reaction and extract rate constants for the individual steps. The simulated data are presented as the solid curves in Figure 3B, and a plot of the residuals (experiment—simulation) is also given. Rate constants (k-values in formal units of min^{-1}, since the mole fraction for all species is dimensionless) and pertinent simulation parameters are gathered in the table (Figure 3, panel B). Overall, the kinetic simulations gave an outstanding fit with the experimental data. The *P*-value of 1.00 and a χ^2 value of 0.9314 indicated that no systematic deviations were observed in the simulations that were beyond the expected signal-to-noise ratio of the experiment.

From the simulated rate constants, it is immediately apparent that the rate determining step for the synthesis of [4]rotaxane **12** formally corresponds to the second CB[6]-accelerated click reaction (k_5 = 0.33 min^{-1}). In contrast, the rate constant for the first click reaction, which produced intermediate **28** ⊃ *β*-CD, is almost one order of magnitude faster (k_3 = 2.84 min^{-1}; an 8.6-fold increase versus k_5). This fits the experimental data whereby the pre-equilibrium steps leading to **1** ⊃ *β*-CD and **2** ⊃ CB[6] are both fast, and rapid formation of the intermediate species (**28** + **28** ⊃ *β*-CD) was observed. For the **1** ⊃ *β*-CD species, the position of equilibrium lies toward the host-guest complex formation (k_1 = 402.94 min^{-1}; k_{-1} = 135.51 min^{-1}), consistent with the ^{1}H-NMR titration data and measurements of the association constant. In contrast, for the **2** ⊃ CB[6] inclusion complex in the full reaction, the position of equilibrium lies slightly toward the side of the separated species (k_2 = 191.84 min^{-1}; k_{-2} = 284.00 min^{-1}), which is consistent with the observation that dissolution of CB[6] is more challenging under the experimental conditions used. Finally, for the intermediate species **28** and **28** ⊃ *β*-CD, the kinetic simulations indicate a strong displacement of the position of equilibrium toward the crucial 3-component molecular inclusion complex **28** ⊃ *β*-CD ($k_4 < 10^{-6}$ and k_{-4} = 24.82 min^{-1}), consistent with our ^{1}H-NMR titration data (supplemental Figure S135 and Table S8). These simulation results also fit the experimental observation that only the desired product **12**, and no byproduct **29**, is produced in the full reaction containing one equivalent of *β*-CD.

Equivalent HPLC chromatograms and a plot showing the experimental change in mole fractions of the various species and the kinetic simulations for the control reaction performed at 50 °C without *β*-CD are presented in Figure 4. The simplest mechanistic pathway for the control reaction that gives homo[3]rotaxane **29**, and which produced the best kinetic simulations of the experimental data using a global fitting algorithm, is presented in Scheme 5. Experimental data associated with the change in the concentration (mole fraction) of compound **1** (green peaks and green square data points), the intermediate [2]semirotaxane **28** (red peaks and red diamond data points), and the homo[3]rotaxane byproduct **29** (yellow peaks and yellow circle data points) are presented in Figure 4, panels A and B. A similar trend is observed in the control reaction in terms of the relative change in concentration of the starting materials, intermediate species, and byproduct as seen for the full reaction. However, it is interesting to note that the control reaction is initially slower

https://doi.org/10.1021/jacs.3c04111
J. Am. Chem. Soc. 2023, 145, 12894−12910

Scheme 4. Reaction Scheme Used in the Kinetic Modeling of the Full Reaction Pathway Leading to the Synthesis of [4]Rotaxane 12 via the [3]Semirotaxane Intermediate 28 ⊃ β-CD

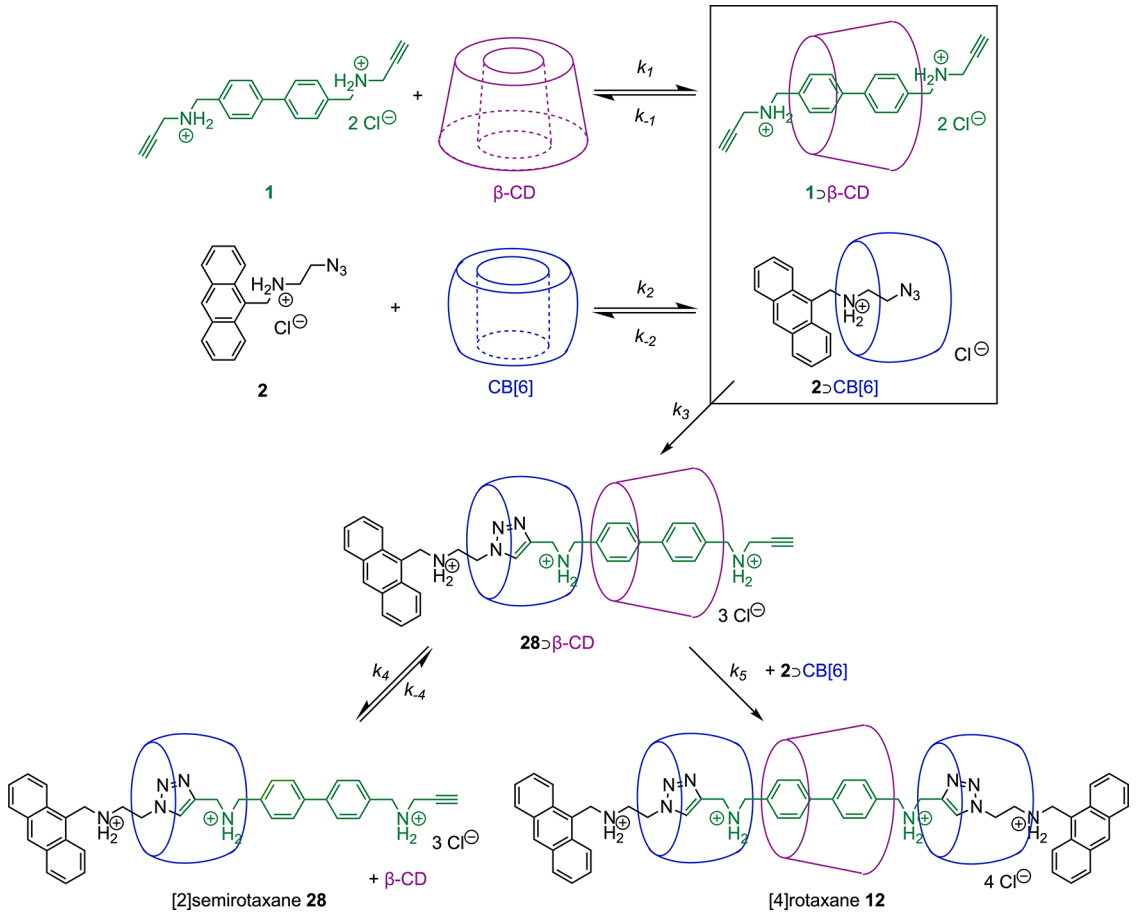

than the full reaction, where the peak in the mole fraction of **28** occurs at the later time point of ∼5 min and the amount of biphenyl-dialkyne **1** continues to decrease throughout the full course of the experiment (30 min). Nevertheless, at 30 min, similar conversion yields are observed whereby the mole fraction of **29** reaches 0.57, whereas in the full reaction, the equivalent value for **12** reaches 0.64 (supplemental Tables S9 and S12). As for the full reaction, the experimental data for the control reaction show a rapid increase and slower decline in the concentration of **28**, which indicates that a stepwise reaction occurs whereby the second CB[6]-accelerated click reaction to give the [3]rotaxane **29** is rate limiting.

Kinetic simulations using the mechanistic pathway represented in Scheme 5 yielded a decent fit between the simulation and experimental data, but at later time points (>15 min), systematic deviations were present that could not be accounted for fully by the model. From the synthetic studies, it was found that [2]semirotaxane **28** decomposed over time at elevated temperatures and that this decomposition is likely to involve a dethreading event. However, attempts to incorporate dethreading of the CB[6] macrocycle from the anthracene-biphenyl axle of **28** in the simulations did not improve the overall fit of the model with the experiment. Given the limitations of the number of species that could be followed, and in the number of data points that were obtained for these control reactions, it is not possible for us to fully resolve the complexity of the decomposition pathways for species **28**. Nevertheless, the kinetic simulations are of sufficient quality to draw several qualitative (and semiquantitative) conclusions. First, the pre-equilibrium between compound **2** and CB[6] reversibly forms the **2** ⊃ CB[6] molecular inclusion complex, which undergoes a rapid click reaction to yield [2]semirotaxane **28** (k_3 = 0.27 min^{-1}). Notably, the first CB[6]-accelerated click reaction is approximately one order of magnitude slower in the control reaction than for the equivalent step observed in the full reaction in the presence of β-CD (k_3 = 2.84 min^{-1}; Figure 3B). This is consistent with the observations of Stoddart and co-workers who noted that the addition of the β-CD[65,66] (or pillararene[67,68]) cofactor increased the efficiency and rate of hetero[4]rotaxane synthesis. Hence, our experimental data provide support for the hypothesis that intermolecular interactions between the β-CD and CB[6] macrocycles have a positive effect on enhancing the rate of triazole synthesis inside the CB[6] cavity. It is important to note here that the experimental data are limited and do not provide any indication as to how or why intermolecular interactions between β-CD and CB[6] influence the rate of the click reaction (see the section on DFT calculations and reaction mechanism below). The rate determining step for the control reaction involves the formation of a 4-component molecular inclusion complex between [2]semirotaxane **28** and **2** ⊃ CB[6]. This rate determining second click step in the control reaction has a rate constant k_5 of 0.17 min^{-1}, which is almost 2-times slower than the equivalent step in the full reaction (k_5 = 0.33 min^{-1}; Figure 3B).

https://doi.org/10.1021/jacs.3c04111
J. Am. Chem. Soc. 2023, 145, 12894−12910

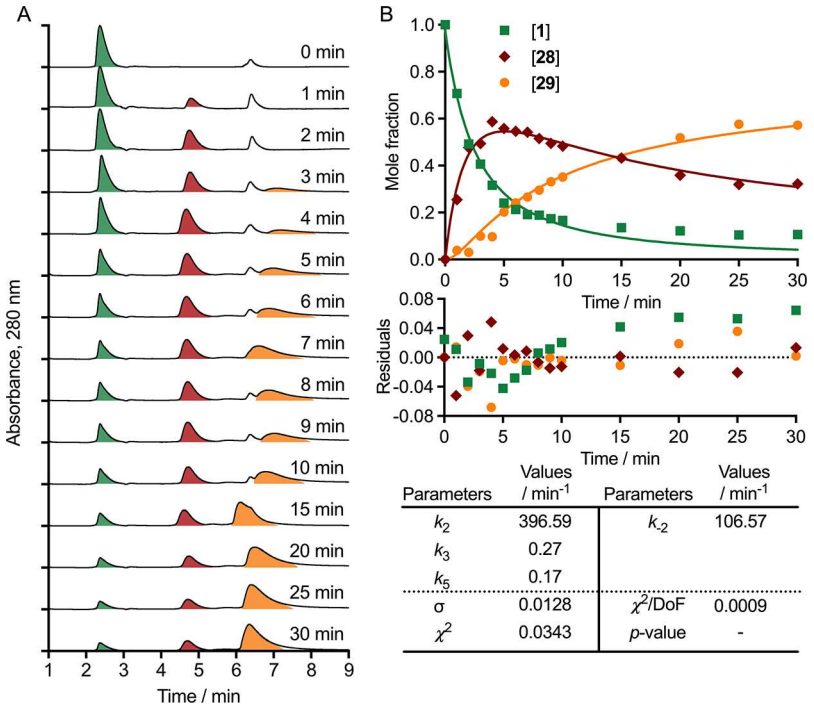

Figure 4. Experimental data and kinetic simulation of the control reaction pathway leading to the synthesis of homo[3]rotaxane **29**. (A) Stack plot showing the evolution of the HPLC profile of the reaction mixture over time for the synthesis of homo[3]rotaxane **29** in H_2O at 50 °C. With reference to the reaction pathway shown in Scheme 5, the peaks highlighted refer to compound **1** (green), the key intermediate [2]semirotaxane **28** (red), and the final product homo[3]rotaxane **29** (yellow). (B) Plot of the experimentally measured mole fractions for the starting material (**1**, green squares), the intermediate (**28**, red diamonds), and product (**29**, yellow circles). Solid lines show the optimum fit of the experimental data obtained by using the kinetic model shown in Scheme 5 with simulations calculated by using *KinTek Global Kinetic Explorer*.

Kinetic studies were also performed at multiple different temperatures (supplemental Figures S136–S139 and Tables S9–S20). Data displaying the change in mole fraction of the various species observed for the full and control reactions recorded at 70, 50, 35, and 23 °C are summarized in supplemental Figure S139. For the full reaction pathway, the conversion yield increased at higher temperature, whereby after 30 min, the mole fraction of **12** increased from 0.294 ± 0.064 (23 °C) to 0.446 ± 0.097 (35 °C), 0.639 ± 0.053 (50 °C), and finally 0.739 ± 0.029 (70 °C). These data demonstrate a linear temperature dependence of the reaction yield when synthesizing [4]rotaxane **12** (supplemental Figure S139, panel J). In contrast, for the control reaction no change in the experimentally measured mole fraction of [3]rotaxane **29** was observed when the temperature increased between 23 and 35 °C, but once again, a linear dependence of the conversion yield was established when the temperature increased between 35 and 70 °C (supplemental Figure S139, panel J). These data indicate that rapid formation of the key intermediate species (**28** ⊃ β-CD for the full reaction and [2]semirotaxane **28** for the control reaction) occurs even at room temperature. However, in the case of the full reaction with β-CD, the rate determining step involving the second triazole synthesis via the 5-component inclusion complex between **28** ⊃ β-CD and **2** ⊃ CB[6] has a lower thermodynamic barrier than the equivalent (4-component) rate determining step in the control reaction, which involves inclusion complex formation between **28** and **2** ⊃ CB[6]. These temperature-dependent data are fully consistent with the mechanistic pathways presented in Schemes 4 and 5, as well as the conclusions drawn from the kinetic simulations where the higher value of the rate constant k_5 for the full versus control reactions suggests a decreased energetic barrier when β-CD is present.

DFT Calculations on the Reaction Mechanism of Rotaxane Synthesis via Cooperative Capture. Experimental data provided clear evidence that formation of the second triazole unit is the rate determining step in synthesis of both the hetero[4]rotaxane **12** and homo[3]rotaxane **29**, and that intermolecular communication occurs between the β-CD and CB[6] macrocycles to enhance the rate and efficiency of the cooperative capture process. Next, we used DFT calculations to explore the mechanisms and energetic landscape of the full and control reactions that lead to rotaxane synthesis. All calculations were performed by using the B3LYP exchange-correlation functionals[101−104] combined with the DGDZVP[105,106] basis set and applying corrections for dispersion effects by using the GD3BJ correction factor.[107−109] In addition, all structures were optimized in the presence of a water continuum solvent model representing the reaction medium used in the experiments. The complete structure of rotaxane **12** is too large to perform full DFT optimization. Therefore, to simplify the calculations and minimize the computational expense, model structures were used in which the anthracene connection to the azide group was replaced, or in selected cases, a truncated biphenyl-alkyne was used as the model guest molecule. For simplicity, a legend showing the calculated structures and corresponding schematics used in the mechanistic schemes and reaction coordinates is shown in Figure 5 panels A and B, respectively. These modifications are remote from the azide-alkyne reaction center and are not anticipated to have an impact on the calculated energetics of the reaction coordinate. As a quick note on the nomenclature that we use in this section, the name **3C-int-1** refers to a

https://doi.org/10.1021/jacs.3c04111
J. Am. Chem. Soc. 2023, 145, 12894−12910

Scheme 5. Reaction Scheme Used in the Kinetic Modeling of the Control Reaction Pathway without β-CD Leading to the Synthesis of Homo[3]rotaxane 29 via the [3]Semirotaxane Intermediate 28

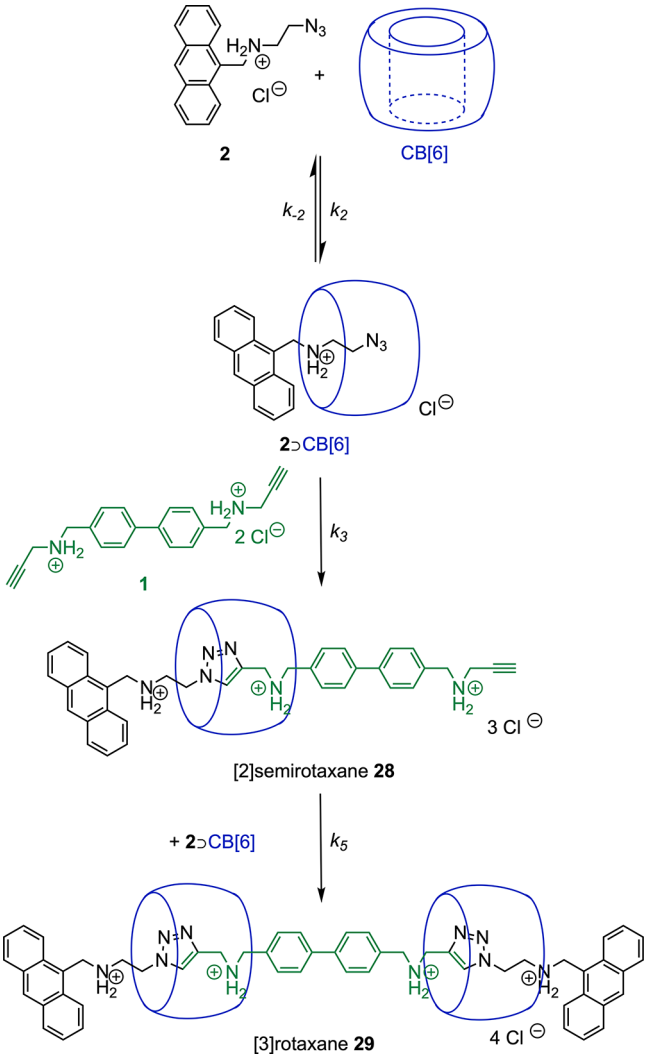

specific, 3-component intermediate (int), which is arbitrarily assigned as species 1. Similarly, the name **4C-TS-1** refers to a particular saddle point on the reaction coordinate that brings together 4 noncovalently attached components in a transition state (TS) and is arbitrarily assigned as the first 4C-TS of this type.

First, we calculated the optimized reaction pathway for the noncatalyzed 1,3-dipolar cycloaddition reaction between the model azide and alkyne components to give the 1,4-substituted triazole product as a baseline (supplemental Figure S140). Overall, the noncatalyzed reaction is thermodynamically feasible with a calculated change in a reaction free energy of $\Delta G = -242$ kJ mol^{-1}, but the reaction has a very high barrier where formation of the transition state involves a change in free energy of $\Delta G_{TS} = +133$ kJ mol^{-1}. The calculated enthalpic change on formation of the transition state is $\Delta H_{TS} = +59$ kJ mol^{-1}, but a large component of energetic barrier arises from the loss of entropy where $-T\Delta S_{TS} = +74$ kJ mol^{-1}.

Next, we used DFT calculations to optimize the structures along the CB[6]-catalyzed azide-alkyne reaction coordinate (supplemental Figure S141). Initially, a reversible 3-component molecular inclusion complex forms (**3C-int-3**, $\Delta G = -114$ kJ mol^{-1}), which brings together the model azide and alkyne units inside the CB[6] macrocyclic cavity. This process is spontaneous whereby the enthalpic change ($\Delta H = -248$ kJ mol^{-1}) compensates for the large loss of entropy ($-T\Delta S = +134$ J K^{-1} mol^{-1}). From the **3C-int-3** molecular inclusion complex, triazole synthesis proceeds via the **3C-TS-1** transition state, which has a free energy barrier of $\Delta\Delta G_{TS} = +52$ kJ mol^{-1}, the origins of which are entirely enthalpic ($\Delta\Delta H_{TS} = +52$ kJ mol^{-1} and $-T\Delta\Delta S_{TS} = -0.3$ kJ mol^{-1}). Overall, triazole synthesis inside the CB[6] cavity has a much lower free energy barrier than the noncatalyzed process, which fits the experimental situation. The subsequent molecular inclusion product **2C-int-5** forms spontaneously from the reagents ($\Delta G = -415$ kJ mol^{-1}), and notably, there is a relatively high barrier ($\Delta\Delta G = +97$ kJ mol^{-1}) to slippage of the CB[6] macrocycle from inclusion of the triazole ring to the biphenyl rings (species **2C-int-7**, $\Delta G = -318$ kJ mol^{-1}). This computed result also fits with the experimental observation from our synthetic and kinetic work in which increased decomposition of **28** was observed at elevated temperatures and the process was assigned to a dethreading mechanism. Overall, our computational data on the CB[6]-catalyzed azide-alkyne reaction are in line with previous DFT studies by Carlqvist and Maseras,[110] who reportedly found no evidence of TS stabilization and also concluded that the main role of CB[6] is to reduce entropic costs by transforming the reaction into a pseudo-unimolecular process via formation of the ternary (3-component, **3C-int-3**) molecular inclusion complex.

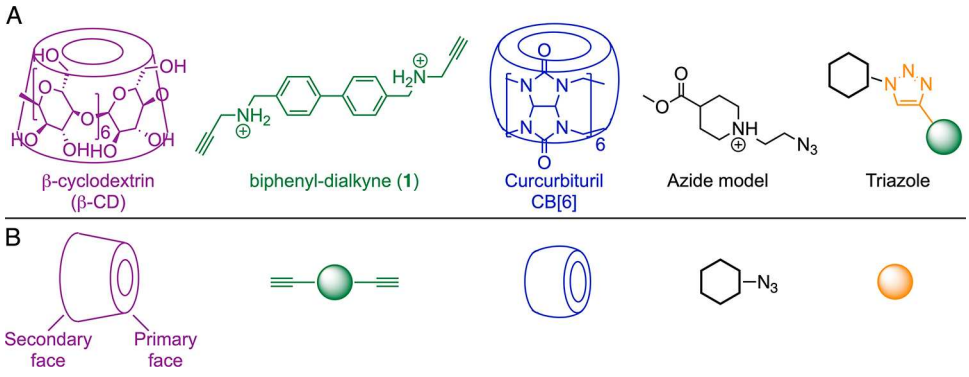

Figure 5. Chemical structures and their equivalent schematic representations for the different species used in the DFT calculations on the mechanism of rotaxane synthesis via cooperative capture. These schematic structures are used in Figures 6–8 for simplicity.

https://doi.org/10.1021/jacs.3c04111
J. Am. Chem. Soc. 2023, 145, 12894–12910

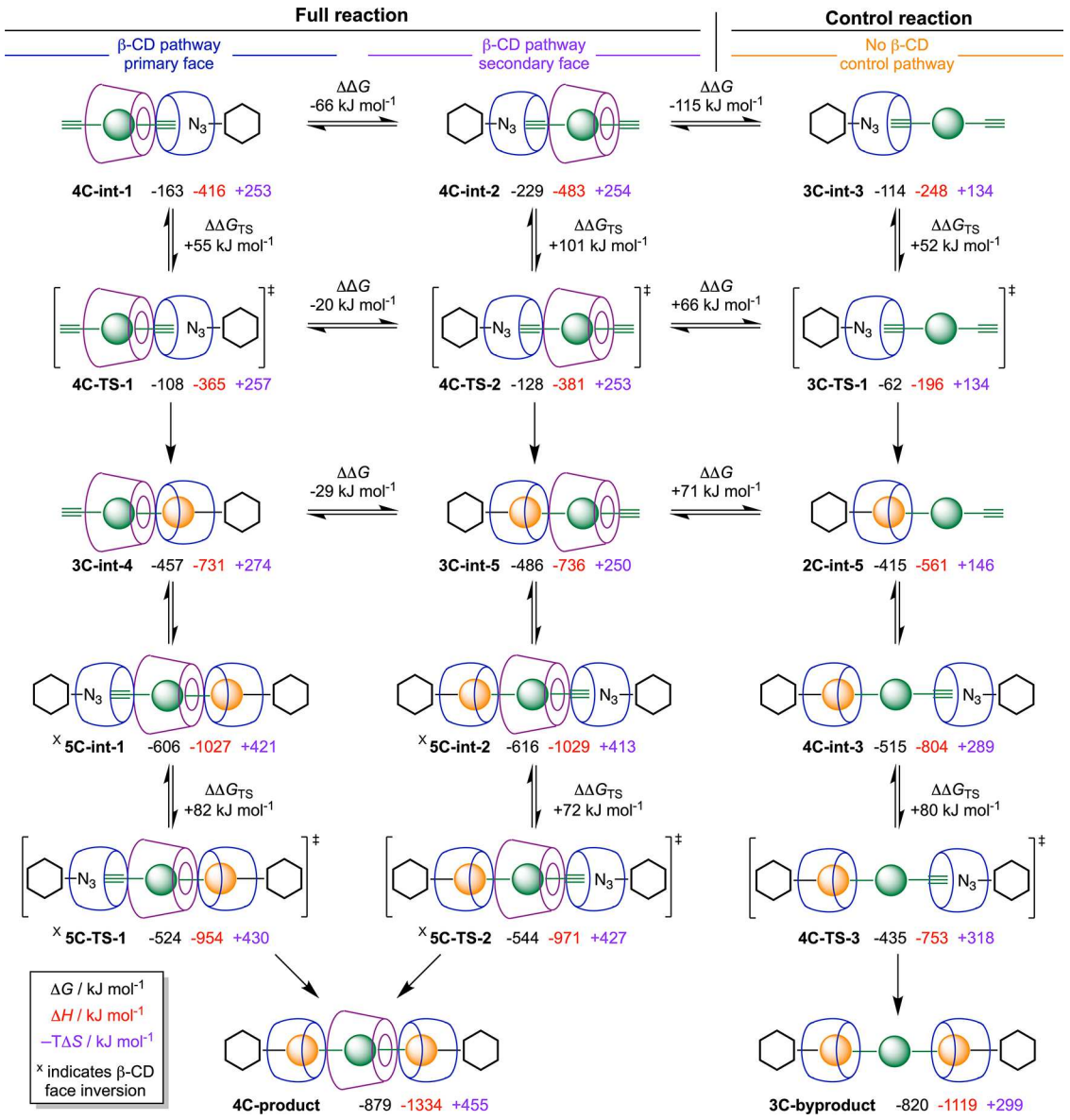

Figure 6. DFT-calculated reaction pathways for the conversion of the starting materials into either the desired **4C-product** via the full reaction involving β-CD or the **3C-byproduct** via the control reaction (without β-CD). Numbers underneath the structures of each species refer to the calculated change in free energy (ΔG/kJ mol^{-1}, black), enthalpy (ΔH/kJ mol^{-1}, red), and entropy ($-T\Delta S$/kJ mol^{-1}, purple), relative to the starting materials. Note that intermediate species ^{X}**5C-int-1** and ^{X}**5C-int-2**, as well as the associated transition states, ^{X}**5C-TS-1**, and ^{X}**5C-TS-2**, involve the CB[6], which resides over the alkyne-azide reaction center, interacting with the opposite face of β-CD from the initial pathway designation (^{X}, β-CD face inversion). See supplemental Figure S142 for the complete pathway including the rapid pre-equilibria steps before the first transition states.

Following on from our baseline calculations, we decided to investigate the complete reaction mechanisms for cooperative capture synthesis of both the model hetero[4]rotaxane (referred to **4C-product** to avoid confusion with the synthetic sections above) and the model homo[3]rotaxane without β-CD (referred to as the **3C-byproduct** for clarity). Details on the critical steps of the reaction mechanisms are presented in Figure 6, and the energetic profiles of three distinct reaction coordinates are presented in Figure 7 (with additional information given in supplemental Figure S142 and Tables S21 and S22). When modeling the full reaction (including the β-CD macrocycle), two alternative reaction pathways emerge. These two pathways are distinguished by the orientation of the β-CD macrocycle with respect to the CB[6]-azide-alkyne reaction center. Specifically, and when considering the first azide-alkyne click step, the primary face of the β-CD macrocycle can either point toward the reaction center (identified as the β-CD primary face pathway shown in blue in Figures 6 and 7) or away from the CB[6] macrocycle (referred to as the β-CD secondary face pathway shown in purple in Figures 6 and 7). Both pathways converge to give the same **4C-product**, but mechanistically, a crossover occurs during the second triazole synthesis step in which the orientation of the β-CD macrocycle appears inverted from the original pathway nomenclature for the intermediate species ^{X}**5C-int-1** and ^{X}**5C-int-2**, as well as the associated transition states ^{X}**5C-TS-1** and ^{X}**5C-TS-2**. Optimized structures, which involve β-CD macrocycle face inversion, are identified with a superscript "x" in Figures 6 and 7. DFT calculations were also

https://doi.org/10.1021/jacs.3c04111
J. Am. Chem. Soc. 2023, 145, 12894−12910

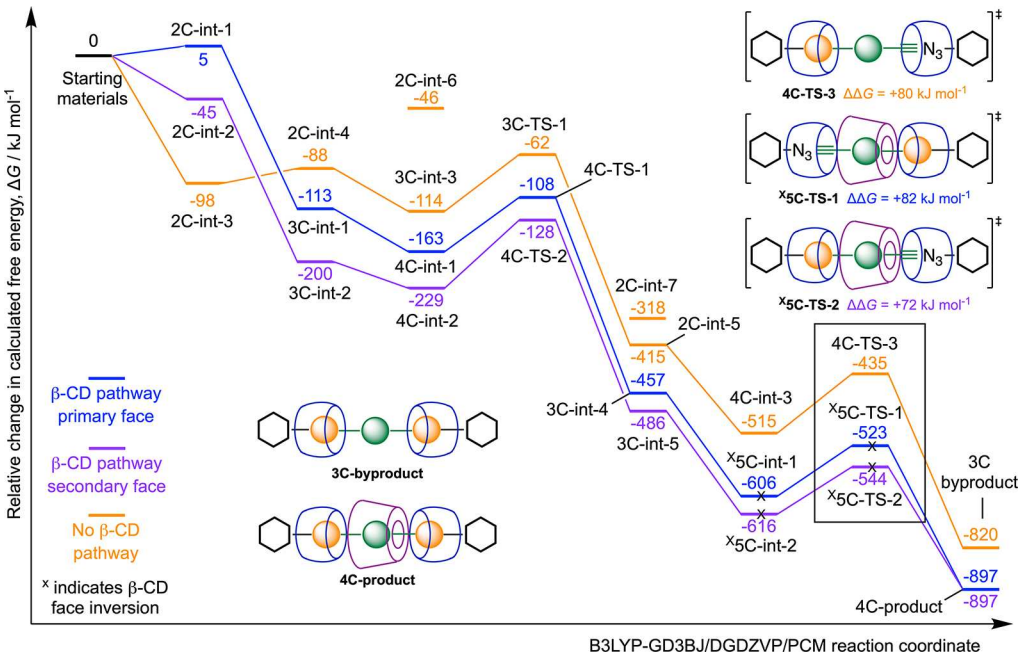

Figure 7. DFT-calculated reaction coordinate showing the change in free energy of the various intermediates and transition states relative to the starting materials for three distinct mechanistic pathways. The full reaction pathway involving an initial CB[6] interaction with the *β*-CD primary face is shown in blue and that with the *β*-CD secondary face is shown in purple. The control reaction without *β*-CD is shown in yellow. Note that intermediate species ^{X}**5C-int-1** and ^{X}**5C-int-2**, as well as the associated transition states, ^{X}**5C-TS-1** and ^{X}**5C-TS-2**, involve the CB[6], which resides over the alkyne-azide reaction center interacting with the opposite face of *β*-CD from the initial pathway designation (^{X}, *β*-CD face inversion).

performed on the model control reaction (without *β*-CD) to give the **3C-byproduct** (Figures 6 and 7, yellow reaction pathway).

Focusing mainly on the full reaction toward the **4C-product**, the *β*-CD primary (blue) and secondary (purple) face pathways both follow the same pattern of steps. Initially, *β*-CD forms inclusion complexes **2C-int-1** or **2C-int-2** with the model biphenyl-alkyne species (supplemental Figure S142). A recurring theme in these mechanistic pathways is that molecular inclusion is enthalpically driven, which provides the energy required to overcome the decrease in entropy. In the next step, the 3-component systems **3C-int-1** and **3C-int-2** form spontaneously via inclusion of the reactive alkyne group inside the CB[6] cavity, which is assisted through stabilizing intermolecular interactions between the *β*-CD and CB[6] macrocycles. Subsequent inclusion of the model azide inside the CB[6] cavity brings together the reacting partners to form intermediates **4C-int-1** (ΔG = −163 kJ mol^{-1}) and **4C-int-2** (ΔG = −229 kJ mol^{-1}). Although the **4C-int-2** species is thermodynamically more stable than **4C-int-1**, the transition-state barrier for the first triazole synthesis via the primary face pathway (**4C-TS-1**, $\Delta\Delta G_{TS}$ = +55 kJ mol^{-1}) is considerably lower than the equivalent barrier found on the secondary face pathway (**4C-TS-2**, $\Delta\Delta G_{TS}$ = +101 kJ mol^{-1}). Given that both pathways are in rapid equilibrium, with facile *β*-CD dethreading and recomplexation expected (from experimental ^{1}H-NMR data), it is likely that the primary face pathway predominates to drive the first click reaction. Interestingly, the **4C-TS-1** free energy barrier is essentially the same as for the calculated baseline reaction with CB[6] but without *β*-CD (Figures 6 and 7, yellow pathway, **3C-TS-1**, $\Delta\Delta G_{TS}$ = +52 kJ mol^{-1}). It should be noted that alternative pathway combinations exist to create the **4C-int-1** and **4C-int-2** species, such as the combination of two separate molecular inclusion complexes involving, for example, **2C-int-1** or **2C-int-2** with the model azide ⊃ CB[6] complex (**2C-int-6**, supplemental Table S14), but for successful reactions, all combinations must eventually pass through one of the early transitions states (**4C-TS-1**, **4C-TS-2**, or **3C-TS-1**), as displayed in Figure 6.

After synthesis of the first triazole, the new intermediates **3C-int-4** (blue pathway) and **3C-int-5** (purple pathway), as well as the no *β*-CD intermediate, **2C-int-5**, (yellow pathway) are in rapid equilibrium via *β*-CD dethreading and recomplexation. Following further association steps, the full reaction pathways eventually arrive at the key 5-component intermediate species, ^{X}**5C-int-1** (blue pathway) and ^{X}**5C-int-2** (purple pathway). It is important to note here that the orientation of the *β*-CD macrocycle is inverted from the original pathway face definition. Synthesis of the second triazole unit can be accomplished from these intermediates through the corresponding transition states, ^{X}**5C-TS-1** and ^{X}**5C-TS-2**. For ^{X}**5C-TS-2**, the primary face of the *β*-CD macrocycle points toward the CB[6]-azide-alkyne reaction center and corresponding free energy barrier, $\Delta\Delta G_{TS}$ = +72 kJ mol^{-1}. In contrast, the calculated transition-state barrier for formation of ^{X}**5C-TS-1** is higher at $\Delta\Delta G_{TS}$ = +82 kJ mol^{-1}. Here, the DFT calculations provide a clear indication that the second click reaction is the rate determining step in the cooperative capture synthesis of **4C-product**, and the reaction occurs preferentially when the primary face of the *β*-CD macrocycle points toward the CB[6]-azide-alkyne reaction center. For comparison, in the control reaction pathway, the second click step passing through the **4C-TS-3** transition-state species is also calculated to be rate determining with a free energy barrier ($\Delta\Delta G_{TS}$ = +80 kJ mol^{-1}) that is +8 kJ mol^{-1} higher than the lowest energy route on the full reaction pathway. After the second click reaction, the **4C-product** is

https://doi.org/10.1021/jacs.3c04111
J. Am. Chem. Soc. 2023, 145, 12894−12910

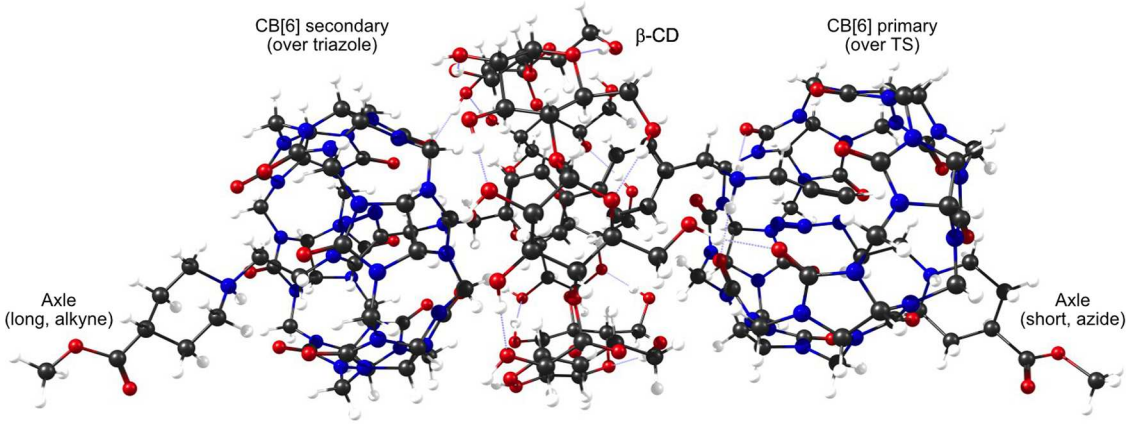

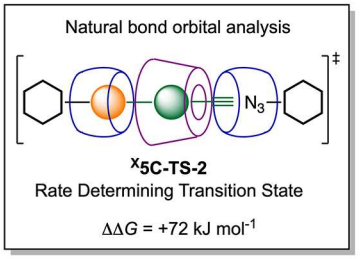

Intermolecular interaction in ^{X}**5C-TS-2**	Intermolecular stabilization energy (ISE) / kJ mol^{-1}	Percentage of total intermolecular stabilization / %	ΔE (^{X}**5C-TS-2** - ^{X}**5C-TS-1**) / kJ mol^{-1}
Total between axle units	571.12	28.57	N/A
Axle-to-rings	304.68	15.24	4.14
Rings-to-axle	827.34	41.39	24.43
Total between rings	295.73	14.79	22.89
Axle-to-CB[6]	223.68	11.19	2.64
Axle-to-β-CD	81.00	4.05	1.51
CB[6]-to-axle	741.53	37.10	19.50
β-CD-to-axle	85.81	4.29	4.94
β-CD-to-CB[6]	122.97	6.15	5.65
CB[6]-to-β-CD	172.76	8.64	17.24
CB[6] (over TS)-to-axle	388.69	19.45	16.02
CB[6] (over triazole)-to-axle	352.82	17.65	3.47

Figure 8. DFT-optimized structure and Natural Bond Orbital (NBO) analysis for the rate determining transition state (^{X}**5C-TS-2**) identified in the cooperative capture synthesis of the desired **4C-product**. Data in the table (inset) indicate the NBO deconvolution of the various intermolecular stabilizing interactions between the axle and macrocyclic rings. The percentage values are given with respect to the total calculated intermolecular stabilization energy, and the values for ΔE refer to the calculated difference between the rate determining transition state ^{X}**5C-TS-2** (where the transition state for triazole formation occurs inside the CB[6] that interacts with the β-CD primary face) and the higher energy transition state ^{X}**5C-TS-1**. Positive values for ΔE indicate that the NBO interaction in ^{X}**5C-TS-2** is stronger than the equivalent intermolecular interaction calculated in ^{X}**5C-TS-1**. Further details on the NBO analysis are presented in the Supporting Information.

formed with an overall change in reaction free energy of ΔG = −879 kJ mol^{-1}. In comparison, the driving force for the synthesis of the **3C-byproduct** on the control reaction pathway (Figures 6 and 7, yellow pathway) is slightly lower with ΔG = −820 kJ mol^{-1}. Overall, these DFT results are in full agreement with the synthetic work, spectroscopy, kinetic experiments, and simulations described above, which confirms that the second click reaction is rate determining and that the presence of β-CD leads to intermolecular cooperativity with the CB[6] macrocycle that reduces the thermodynamic barrier and increases both reaction rates and conversion yields.

These calculations help to answer the question of "why" β-CD enhances the cooperative capture synthesis of hetero[4]-rotaxanes—essentially through enthalpic stabilization of the key intermediates and transitions states, which drives the positions of equilibria toward the β-CD molecular inclusion routes—but they do not address "how" this energetic preference arises. Therefore, we used Natural Bond Orbital (NBO) analysis to investigate the intermolecular stabilization interactions present in the key transition states, ^{X}**5C-TS-1**, ^{X}**5C-TS-2**, and **4C-TS-3**, as well as the **4C-product** and **3C-byproduct**, in an attempt to identify the origins of the intermolecular interactions that control the observed differences in rate between the full and control reactions.

Natural Bond Orbital (NBO) Analysis of the Rate Determining Transition State. A detailed analysis of the results from the NBO calculations on the rate determining transition state, ^{X}**5C-TS-2**, located on the full reaction pathway (Figures 6 and 7, purple) is presented in Figure 8. Equivalent analyses for the ^{X}**5C-TS-1**, **4C-TS-3**, **4C-product**, and **3C-byproduct** species are presented in the Supporting Information.

For ^{X}**5C-TS-2**, NBO analysis revealed that intermolecular stabilizing interactions between the two components of the axle (azide [short] and alkyne [long], Figure 8), between the axle and macrocyclic rings, and interactions between the β-CD and CB[6] rings account for 2.50% of the total stabilization energy of the molecule. The remaining 97.5% is assigned to discrete covalent bonds within the five separate components. This intermolecular stabilization energy (ISE) is relatively high, which provides the enthalpic driving force for spontaneous self-assembly and outweighs the loss of entropy incurred on bringing five species together. As expected for a transition state leading to the triazole product via 1,3-dipolar cycloaddition, intermolecular interactions between the azide and alkyne components contribute 28.57% of the total ISE. The remaining 71.42% of total ISE involves intermolecular interactions from the axle units to the rings (15.24%), from the rings to the axle units (41.39%), and between the β-CD and CB[6] rings (14.79%). As can be seen from the deconvolution of NBO interactions, donation of electron density from the CB[6] to axle dominates (37.10% of ISE). In contrast, intermolecular interactions from the biphenyl group of the axle (long) to β-CD and *vice versa* from β-CD to the biphenyl

https://doi.org/10.1021/jacs.3c04111
J. Am. Chem. Soc. 2023, 145, 12894−12910

contribute only 4.05 and 4.29%, respectively (total ISE(axle/β-CD) = 8.35%). This observation is consistent with the experimental work and DFT calculations on the mechanism, which showed that ring slippage and dethreading of the CB[6] macrocycle requires elevated temperatures, whereas the molecular inclusion complex **1** ⊃ β-CD is in rapid equilibrium with unbound species at room temperature. Interestingly, the CB[6] macrocycle that interacts with the azide-alkyne transition state contributes essentially the same amount of energy to the total ISE (19.45%) of ^{X}**5C-TS-2** as the CB[6] ring that sits over the triazole unit (17.65%). This is also consistent with the conclusions of Carlqvist and Maseras[110] who determined that TS stabilization by CB[6] plays a minor role in the catalytic acceleration of the azide-alkyne reaction. Intermolecular interactions from the β-CD-to-CB[6] rings and *vice versa* from CB[6]-to-β-CD rings account for 6.15 and 8.64% of the total ISE, respectively. Of these inter-ring interactions, the closer (spatial) approach of CB[6] with the secondary face of the β-CD leads to stronger intermolecular stabilization (9.25% of total ISE) than between CB[6] and the β-CD primary face (5.55% of total ISE). The NBO calculations suggest that the role of β-CD in increasing the rate and efficiency of hetero[4]rotaxane synthesis via cooperative capture arises due to relatively minor intermolecular interactions with the CB[6] rings that help to reduce entropic freedom within the key (rate determining) transition state, ^{X}**5C-TS-2**. Rigidifying the 5-component structure likely increases the barrier to rotation of the macrocyclic rings, but also increased stabilizing interactions between the rings has the effect of displacing the position of equilibrium toward the 5-component intermediate, and hence, increasing the likelihood of successful triazole (and hetero[4]rotaxane) synthesis.

CONCLUSIONS

Experimental data exploring the synthesis and chemical scope of functionalized hetero[4]rotaxanes illustrate that a variety of substituted β-CD macrocyclic rings featuring electrophilic leaving groups, carboxylates, and azides can be used to introduce reactive groups that facilitate further derivatization with biological active vectors. Importantly, the azide species can react via classic copper ion-mediated or strain-promoted click chemistry providing further options for using bioorthogonal chemistry to create bioactive rotaxanes. Synthetic work also demonstrated that care must be taken in the choice of both the conjugation chemistry and nature of the substituents added to the monofunctionalized β-CD macrocycle. Detailed kinetic studies on a model system revealed that the rate determining step in the multicomponent cooperative capture of both hetero[4]rotaxanes and the homo[3]rotaxanes (without β-CD) corresponds to the second CB[6]-mediated azide-alkyne click reaction. Kinetic simulations provided insights into the mechanism of the cooperative capture, and extensive DFT calculations on the various reaction pathways confirmed the conclusions drawn from the experiments. The self-assembly of rotaxanes through cooperative capture involves enthalpically driven molecular inclusion, which compensates for the dramatic decrease in entropy that occurs when up to 5 separate components converge in the critical rate determining transition states. Thermodynamic analysis confirmed that the main role of CB[6] in accelerating triazole synthesis is not through stabilization of the transition state but rather through compensation of the entropic penalty through formation of a molecular inclusion complex, which effectively transforms the reaction into a pseudo-unimolecular process. DFT calculations also revealed a mechanistic preference in which intermolecular interactions between the primary face of β-CD and the CB[6] macrocycle that resides over the azide-alkyne transition state leads to faster triazole synthesis than the equivalent interactions via the β-CD secondary face. Bonding analysis also showed that relatively minor intermolecular interactions between the CB[6] and β-CD macrocycles are responsible for rigidifying the transition state, which experimentally has the effect of increasing the rate of reaction, and the efficiency or yield, of rotaxane synthesis. Collectively, our synthetic, kinetic, and computational data reveal new insights into the mechanism of cooperative capture rotaxane synthesis and demonstrate new possibilities for developing this exciting molecularly interlocked scaffold into bioactive compounds.

ASSOCIATED CONTENT

Supporting Information

The Supporting Information is available free of charge at https://pubs.acs.org/doi/10.1021/jacs.3c04111.

Experimental details, HPLC chromatograms, NMR spectra, and high-resolution mass spectrometry data for all new compounds, data from the kinetic experiments and computational details including the calculated thermodynamics, NBO analysis, and Cartesian coordinates of all-optimized structures (PDF)

AUTHOR INFORMATION

Corresponding Author

Jason P. Holland − *Department of Chemistry, University of Zurich, Zurich CH-8057, Switzerland;* orcid.org/0000-0002-0066-219X; Phone: +41-44-63-53990; Email: jason.holland@chem.uzh.ch

Author

Faustine d'Orchymont − *Department of Chemistry, University of Zurich, Zurich CH-8057, Switzerland;* orcid.org/0000-0002-3726-1648

Complete contact information is available at: https://pubs.acs.org/10.1021/jacs.3c04111

Notes

The authors declare no competing financial interest.

ACKNOWLEDGMENTS

J.P.H. is supported by the Swiss National Science Foundation (SNSF Professorship PP00P2_163683 and PP00P2_190093) and the University of Zurich (UZH). F.d'O. received a Swiss Government Excellence Scholarship (ESKAS-Nr: 2017.0043). This project has received funding (in part) from the European Union's Horizon 2020 research and innovation programme/ from the European Research Council under the Grant Agreement numbers 676904, ERC-StG-2015, NanoSCAN, and 101001734, ERC-CoG-2020, PhotoPHARMA. We thank all members of the Holland group for helpful discussions and continuous support. We thank Prof. Michal Juricek and Prof. Oliver Zerbe for helpful discussions.

REFERENCES

(1) Fujita, D.; Ueda, Y.; Sato, S.; Mizuno, N.; Kumasaka, T.; Fujita, M. Self-Assembly of Tetravalent Goldberg Polyhedra from 144 Small Components. *Nature* **2016**, *540*, 563−566.

(2) Bruns, C. J.; Stoddart, J. F. *The Nature of the Mechanical Bond*; Wiley: Hoboken, 2016.
(3) Neal, E. A.; Goldup, S. M. Chemical Consequences of Mechanical Bonding in Catenanes and Rotaxanes: Isomerism, Modification, Catalysis and Molecular Machines for Synthesis. *Chem. Commun.* **2014**, *50*, 5128−5142.
(4) Livoreil, A.; Dietrich-Buchecker, C.; Sauvage, J. Electrochemically Triggerred Swinging of a [2]Catenate. *J. Am. Chem. Soc.* **1994**, *116*, 9399−9400.
(5) Bissell, R. A.; Cordova, E.; Kaifer, A. E.; Stoddart, J. F. A Chemically and Electrochemically Switchable Molecular Shuttle. *Nature* **1994**, *369*, 133−137.
(6) Erbas-Cakmak, S.; Leigh, D. A.; McTernan, C. T.; Nussbaumer, A. L. Artificial Molecular Machines. *Chem. Rev.* **2015**, *115*, 10081−10206.
(7) Fletcher, S. P.; Dumur, F.; Pollard, M. M.; Feringa, B. L. A Reversible, Unidirectional Molecular Rotary Motor Driven by Chemical Energy. *Science* **2005**, *310*, 80−82.
(8) Luo, Y.; Collier, C. P.; Jeppesen, J. O.; Nielsen, K. A.; DeIonno, E.; Ho, G.; Perkins, J.; Tseng, H. R.; Yamamoto, T.; Stoddart, J. F.; Heath, J. R. Two-Dimensional Molecular Electronics Circuits. *ChemPhysChem* **2002**, *3*, 519−525.
(9) Galli, M.; Lewis, J. E. M.; Goldup, S. M. A Stimuli-Responsive Rotaxane-Gold Catalyst: Regulation of Activity and Diastereoselectivity. *Angew. Chem., Int. Ed.* **2015**, *54*, 13545−13549.
(10) Heard, A. W.; Goldup, S. M. Synthesis of a Mechanically Planar Chiral Rotaxane Ligand for Enantioselective Catalysis. *Chem* **2020**, *6*, 994−1006.
(11) Cirulli, M.; Salvadori, E.; Zhang, Z. H.; Dommett, M.; Tuna, F.; Bamberger, H.; Lewis, J. E. M.; Kaur, A.; Tizzard, G. J.; van Slageren, J.; Crespo-Otero, R.; Goldup, S. M.; Roessler, M. M. Rotaxane CoII Complexes as Field-Induced Single-Ion Magnets. *Angew. Chem., Int. Ed.* **2021**, *60*, 16051−16058.
(12) Ma, X.; Zhao, Y. Biomedical Applications of Supramolecular Systems Based on Host-Guest Interactions. *Chem. Rev.* **2015**, *115*, 7794−7839.
(13) Dong, R.; Zhou, Y.; Huang, X.; Zhu, X.; Lu, Y.; Shen, J. Functional Supramolecular Polymers for Biomedical Applications. *Adv. Mater.* **2015**, *27*, 498−526.
(14) Pairault, N.; Barat, R.; Tranoy-Opalinski, I.; Renoux, B.; Thomas, M.; Papot, S. Rotaxane-Based Architectures for Biological Applications. *Comptes Rendus Chim.* **2016**, *19*, 103.
(15) Casini, A.; Woods, B.; Wenzel, M. The Promise of Self-Assembled 3D Supramolecular Coordination Complexes for Biomedical Applications. *Inorg. Chem.* **2017**, *56*, 14715−14729.
(16) Webber, M. J.; Langer, R. Drug Delivery by Supramolecular Design. *Chem. Soc. Rev.* **2017**, *46*, 6600−6620.
(17) Pöthig, A.; Casini, A. Recent Developments of Supramolecular Metal-Based Structures for Applications in Cancer Therapy and Imaging. *Theranostics* **2019**, *9*, 3150−3169.
(18) Riebe, J.; Niemeyer, J. Mechanically Interlocked Molecules for Biomedical Applications. *Eur. J. Org. Chem.* **2021**, *2021*, 5106−5116.
(19) Moreno-Alcántar, G.; Casini, A. Bioinorganic Supramolecular Coordination Complexes and Their Biomedical Applications. *FEBS Lett.* **2023**, 1−202.
(20) Wang, Z.; Sun, C.; Yang, K.; Chen, X.; Wang, R. Cucurbituril-Based Supramolecular Polymers for Biomedical Applications. *Angew. Chem., Int. Ed.* **2022**, *61*, No. e202206763.
(21) Schröder, H. V.; Zhang, Y.; Link, A. J. Dynamic Covalent Self-Assembly of Mechanically Interlocked Molecules Solely Made from Peptides. *Nat. Chem.* **2021**, *13*, 850−857.
(22) Katayev, E. A.; Kolesnikov, G. V.; Khrustalev, V. N.; Antipin, M. Y.; Askerov, R. K.; Maharramov, A. M.; German, K. E.; Kirakosyan, G. A.; Tananaev, I. G.; Timofeeva, T. V. Recognition of Perrhenate and Pertechnetate by a Neutral Macrocyclic Receptor. *J. Radioanal. Nucl. Chem.* **2009**, *282*, 385−389.
(23) Katayev, E. A.; Kolesnikov, G. V.; Sessler, J. L. Molecular Recognition of Pertechnetate and Perrhenate. *Chem. Soc. Rev.* **2009**, *38*, 1572−1586.
(24) Alberto, R.; Bergamaschi, G.; Braband, H.; Fox, T.; Amendola, V. TcO_4^-: Selective Recognition and Trapping in Aqueous Solution. *Angew. Chem., Int. Ed.* **2012**, *51*, 9772−9776.
(25) Amendola, V.; Alberti, G.; Bergamaschi, G.; Biesuz, R.; Boiocchi, M.; Ferrito, S.; Schmidtchen, F. P. Cavity Effect on Perrhenate Recognition by Polyammonium Cages. *Eur. J. Inorg. Chem.* **2012**, *21*, 3410−3417.
(26) Lewis, J. E. M.; Gavey, E. L.; Cameron, S. A.; Crowley, J. D. Stimuli-Responsive Pd_2L_4 Metallosupramolecular Cages: Towards Targeted Cisplatin Drug Delivery. *Chem. Sci.* **2012**, *3*, 778−784.
(27) Schmidt, A.; Molano, V.; Hollering, M.; Pöthig, A.; Casini, A.; Kühn, F. E. Evaluation of New Palladium Cages as Potential Delivery Systems for the Anticancer Drug Cisplatin. *Chem. − Eur. J.* **2016**, *22*, 2253−2256.
(28) Han, J.; Schmidt, A.; Zhang, T.; Permentier, H.; Groothuis, G. M. M.; Bischoff, R.; Kühn, F. E.; Horvatovich, P.; Casini, A. Bioconjugation Strategies to Couple Supramolecular: Exo-Functionalized Palladium Cages to Peptides for Biomedical Applications. *Chem. Commun.* **2017**, *53*, 1405−1408.
(29) Yue, Z.; Wang, H.; Li, Y.; Qin, Y.; Xu, L.; Bowers, D. J.; Gangoda, M.; Li, X.; Yang, H. B.; Zheng, Y. R. Coordination-Driven Self-Assembly of a Pt(IV) Prodrug-Conjugated Supramolecular Hexagon. *Chem. Commun.* **2018**, *54*, 731−734.
(30) Sawada, T.; Inomata, Y.; Shimokawa, K.; Fujita, M. A Metal-Peptide Capsule by Multiple Ring Threading. *Nat. Commun.* **2019**, *10*, 5687.
(31) Woods, B.; Silva, R. D. M.; Schmidt, C.; Wragg, D.; Cavaco, M.; Neves, V.; Ferreira, V. F. C.; Gano, L.; Morais, T. S.; Mendes, F.; Correia, J. D. G.; Casini, A. Bioconjugate Supramolecular Pd^{2+} Metallacages Penetrate the Blood Brain Barrier In Vitro and In Vivo. *Bioconjugate Chem.* **2021**, *32*, 1399−1408.
(32) Cosialls, R.; Simó, C.; Borros, S.; Gçomez-Vallejo, V.; Schmidt, C.; Llop, J.; Cuenca, A. B.; Casini, A. PET Imaging of Self-assembled ^{18}F-labelled Pd_2L_4 Metallacages for Anticancer Drug Delivery. *Chem. − Eur. J.* **2022**, *18*, No. e202202604.
(33) Therrien, B.; Süss-Fink, G.; Govindaswamy, P.; Renfrew, A. K.; Dyson, P. J. The "Complex-in-a-Complex" Cations $[(Acac)_2MC\ Ru_6(p\text{-}IPrC_6H_4Me)_6(Tpt)\ 2(Dhbq)_3]^{6+}$: A Trojan Horse for Cancer Cells. *Angew. Chem., Int. Ed.* **2008**, *47*, 3773−3776.
(34) Xue, M.; Yang, Y.; Chi, X.; Yan, X.; Huang, F. Development of Pseudorotaxanes and Rotaxanes: From Synthesis to Stimuli-Responsive Motions to Applications. *Chem. Rev.* **2015**, *115*, 7398−7501.
(35) Niu, Z.; Gibson, H. W. Polycatenanes. *Chem. Rev.* **2009**, *109*, 6024−6046.
(36) Evans, N. H.; Beer, P. D. Progress in the Synthesis and Exploitation of Catenanes since the Millennium. *Chem. Soc. Rev.* **2014**, *43*, 4658−4683.
(37) Mena-Hernando, S.; Pérez, E. M. Mechanically Interlocked Materials. Rotaxanes and Catenanes beyond the Small Molecule. *Chem. Soc. Rev.* **2019**, *48*, 5016−5032.
(38) Gil-Ramírez, G.; Leigh, D. A.; Stephens, A. J. Catenanes: Fifty Years of Molecular Links. *Angew. Chem., Int. Ed.* **2015**, *54*, 6110−6150.
(39) Barat, R.; Legigan, T.; Tranoy-Opalinski, I.; Renoux, B.; Péraudeau, E.; Clarhaut, J.; Poinot, P.; Fernandes, A. E.; Aucagne, V.; Leigh, D. A.; Papot, S. A Mechanically Interlocked Molecular System Programmed for the Delivery of an Anticancer Drug. *Chem. Sci.* **2015**, *6*, 2608−2613.
(40) Zhang, J.; Ma, P. X. Cyclodextrin-Based Supramolecular Systems for Drug Delivery : Recent Progress and Future Perspective. *Adv. Drug Delivery Rev.* **2013**, *65*, 1215−1233.
(41) Angelos, S.; Yang, Y.-W.; Patel, K.; Stoddart, J. F.; Zink, J. I. PH-Responsive Supramolecular Nanovalves Based on Cucurbi[6]Uril Pseudorotaxanes. *Angew. Chem., Int. Ed.* **2008**, *120*, 2254−2258.
(42) Simões, S. M. N.; Rey-Rico, A.; Concheiro, A.; Alvarez-Lorenzo, C. Supramolecular Cyclodextrin-Based Drug Nanocarriers. *Chem. Commun.* **2015**, *51*, 6275−6289.

https://doi.org/10.1021/jacs.3c04111
J. Am. Chem. Soc. 2023, 145, 12894−12910

(43) Wang, X.; Smithrud, D. B. Pt-Rotaxanes as Cytotoxic Agents. *Bioorg. Med. Chem. Lett.* **2011**, *21*, 6880−6883.
(44) Smithrud, D. B.; Powers, L.; Lunn, J.; Abernathy, S.; Peschka, M.; Ho, S. M.; Tarapore, P. Ca^{2+} Selective Host Rotaxane Is Highly Toxic Against Prostate Cancer Cells. *ACS Med. Chem. Lett.* **2017**, *8*, 163−167.
(45) Sojka, M.; Fojtu, M.; Fialova, J.; Masarik, M.; Necas, M.; Marek, R. Locked and Loaded: Ruthenium(II)-Capped Cucurbit[n]-Uril-Based Rotaxanes with Antimetastatic Properties. *Inorg. Chem.* **2019**, *58*, 10861−10870.
(46) Hannon, M. J. Supramolecular DNA Recognition. *Chem. Soc. Rev.* **2007**, *36*, 280−295.
(47) Kench, T.; Summers, P. A.; Kuimova, M. K.; Lewis, J. E. M.; Vilar, R. Rotaxanes as Cages to Control DNA Binding, Cytotoxicity, and Cellular Uptake of a Small Molecule**. *Angew. Chem., Int. Ed.* **2021**, *60*, 10928−10934.
(48) Burke, B. P.; Grantham, W.; Burke, M. J.; Nichol, G. S.; Roberts, D.; Renard, I.; Hargreaves, R.; Cawthorne, C.; Archibald, S. J.; Lusby, P. J. Visualizing Kinetically Robust $Co^{III}_4L_6$ Assemblies In Vivo: SPECT Imaging of the Encapsulated $[^{99m}Tc]TcO_4^-$ Anion. *J. Am. Chem. Soc.* **2018**, *140*, 16877−16881.
(49) Arunkumar, E.; Fu, N.; Smith, B. D. Squaraine-Derived Rotaxanes : Highly Stable, Fluorescent Near-IR Dyes. *Chem. − Eur. J.* **2006**, *12*, 4684−4690.
(50) Gassensmith, J. J.; Baumes, J. M.; Smith, B. D. Discovery and Early Development of Squaraine Rotaxanes. *Chem. Commun.* **2009**, *42*, 6329−6338.
(51) Zhai, C.; Schreiber, C. L.; Padilla-coley, S.; Oliver, A. G.; Smith, B. D. Fluorescent Self-Threaded Peptide Probes for Biological Imaging Research Articles. *Angew. Chem., Int. Ed.* **2020**, *59*, 23740−23747.
(52) Fredy, J. W.; Scelle, J.; Guenet, A.; Morel, E.; Adam De Beaumais, S.; Ménand, M.; Marvaud, V.; Bonnet, C. S.; Tóth, E.; Sollogoub, M.; Vives, G.; Hasenknopf, B. Cyclodextrin Polyrotaxanes as a Highly Modular Platform for the Development of Imaging Agents. *Chem. − Eur. J.* **2014**, *20*, 10915−10920.
(53) Fredy, J. W.; Scelle, J.; Ramniceanu, G.; Doan, B. T.; Bonnet, C. S.; Tóth, É.; Ménand, M.; Sollogoub, M.; Vives, G.; Hasenknopf, B. Mechanostereoselective One-Pot Synthesis of Functionalized Head-to-Head Cyclodextrin [3]Rotaxanes and Their Application as Magnetic Resonance Imaging Contrast Agents. *Org. Lett.* **2017**, *19*, 1136−1139.
(54) Hou, S.; Choi, J. S.; Garcia, M. A.; Xing, Y.; Chen, K. J.; Chen, Y. M.; Jiang, Z. K.; Ro, T.; Wu, L.; Stout, D. B.; Tomlinson, J. S.; Wang, H.; Chen, K.; Tseng, H. R.; Lin, W. Y. Pretargeted Positron Emission Tomography Imaging That Employs Supramolecular Nanoparticles with in Vivo Bioorthogonal Chemistry. *ACS Nano* **2016**, *10*, 1417−1424.
(55) Ge, H.; Riss, P. J.; Mirabello, V.; Calatayud, D. G.; Flower, S. E.; Arrowsmith, R. L.; Fryer, T. D.; Hong, Y.; Sawiak, S.; Jacobs, R. M. J.; Botchway, S. W.; Tyrrell, R. M.; James, T. D.; Fossey, J. S.; Dilworth, J. R.; Aigbirhio, F. I.; Pascu, S. I. Behavior of Supramolecular Assemblies of Radiometal-Filled and Fluorescent Carbon Nanocapsules In Vitro and In Vivo. *Chem* **2017**, *3*, 437−460.
(56) Geng, W.-C.; Zheng, Z.; Guo, D.-S. Supramolecular Design Based Activatable Magnetic Resonance Imaging. *View* **2021**, *2*, 20200059.
(57) Lee, H.; Shahrivarkevishahi, A.; Lumata, J. L.; Luzuriaga, M. A.; Hagge, L. M.; Benjamin, C. E.; Brohlin, O. R.; Parish, C. R.; Firouzi, H. R.; Nielsen, S. O.; Lumata, L. L.; Gassensmith, J. J. Supramolecular and Biomacromolecular Enhancement of Metal-Free Magnetic Resonance Imaging Contrast Agents. *Chem. Sci.* **2020**, *11*, 2045−2050.
(58) Oshovsky, G. V.; Reinhoudt, D. N.; Verboom, W. Supramolecular Chemistry in Water. *Angew. Chem., Int. Ed.* **2007**, *46*, 2366−2393.
(59) Yu, G.; Wu, D.; Li, Y.; Zhang, Z.; Shao, L.; Zhou, J.; Hu, Q.; Tang, G.; Huang, F. A Pillar[5]Arene-Based [2]Rotaxane Lights up Mitochondria. *Chem. Sci.* **2016**, *7*, 3017−3024.
(60) Fernandes, A.; Viterisi, A.; Coutrot, F.; Potok, S.; Leigh, D. A.; Aucagne, V.; Papot, S. Rotaxane-Based Propeptides: Protection and Enzymatic Release of a Bioactive Pentapeptide. *Angew. Chem., Int. Ed.* **2009**, *48*, 6443−6447.
(61) Fernandes, A.; Viterisi, A.; Aucagne, V.; Leigh, D. A.; Papot, S. Second Generation Specific-Enzyme-Activated Rotaxane Propeptides. *Chem. Commun.* **2012**, *48*, 2083−2085.
(62) Bruns, C. J.; Liu, H.; Francis, M. B. Near-Quantitative Aqueous Synthesis of Rotaxanes via Bioconjugation to Oligopeptides and Proteins. *J. Am. Chem. Soc.* **2016**, *138*, 15307−15310.
(63) d'Orchymont, F.; Holland, J. P. Supramolecular Rotaxane-Based Multi-Modal Probes for Cancer Biomarker Imaging. *Angew. Chem., Int. Ed.* **2022**, No. e202204072.
(64) d'Orchymont, F.; Holland, J. P. A Rotaxane-Based Platform for Tailoring the Pharmacokinetics of Cancer-Targeted Radiotracers. *Chem. Sci.* **2022**, *13*, 12713−12725.
(65) Ke, C.; Smaldone, R. A.; Kikuchi, T.; Li, H.; Davis, A. P.; Stoddart, J. F. Quantitative Emergence of Hetero[4]Rotaxanes by Template-Directed Click Chemistry. *Angew. Chem., Int. Ed.* **2013**, *52*, 381−387.
(66) Hou, X.; Ke, C.; Fraser Stoddart, J. Cooperative Capture Synthesis: Yet Another Playground for Copper-Free Click Chemistry. *Chem. Soc. Rev.* **2016**, *45*, 3766−3780.
(67) Ke, C.; Strutt, N. L.; Li, H.; Hou, X.; Hartlieb, K. J.; McGonigal, P. R.; Ma, Z.; Iehl, J.; Stern, C. L.; Cheng, C.; Zhu, Z.; Vermeulen, N. A.; Meade, T. J.; Botros, Y. Y.; Stoddart, J. F. Pillar[5]Arene as a Co-Factor in Templating Rotaxane Formation. *J. Am. Chem. Soc.* **2013**, *135*, 17019−17030.
(68) Hou, X.; Ke, C.; Cheng, C.; Song, N.; Blackburn, A. K.; Sarjeant, A. A.; Botros, Y. Y.; Yang, Y.-W.; Stoddart, J. F. Efficient Syntheses of Pillar[6]Arene-Based Hetero[4]Rotaxanes Using a Cooperative Capture Strategy. *Chem. Commun.* **2014**, *50*, 6196−6199.
(69) Assaf, K. I.; Nau, W. M. Cucurbiturils: From Synthesis to High-Affinity Binding and Catalysis. *Chem. Soc. Rev.* **2015**, *44*, 394−418.
(70) Tang, B.; Zhao, J.; Xu, J. F.; Zhang, X. Cucurbit[n]Urils for Supramolecular Catalysis. *Chem. − Eur. J.* **2020**, *26*, 15446−15460.
(71) Mock, W. L.; Shih, N. Y. Host-Guest Binding Capacity of Cucurbituril. *J. Org. Chem.* **1983**, *48*, 3618−3619.
(72) Mock, W. L.; Irra, T. A.; Wepsiec, J. P.; Manimaran, T. L. Cycloaddition Induced by Cucurbituril. A Case of Pauling Principle Catalysis. *J. Org. Chem.* **1983**, *48*, 3619−3620.
(73) Mock, W. L.; Irra, T. A.; Wepsiec, J. P.; Adhya, M. Catalysis by Cucurbituril. The Significance of Bound-Substrate Destabilization for Induced Triazole Formation. *J. Org. Chem.* **1989**, *54*, 5302−5308.
(74) Szejtli, J. *Cyclodextrin Technology*; Springer Science and Business Media LLC: London 1988.
(75) Khan, A. R.; Forgo, P.; Stine, K. J.; D'Souza, V. T. Methods for Selective Modifications of Cyclodextrins. *Chem. Rev.* **1998**, *98*, 1977−1996.
(76) Hybl, A.; Rundle, R. E.; Williams, D. E. The Crystal and Molecular Structure of the Cyclohexaamylose-Potassium Acetate Complex. *J. Am. Chem. Soc.* **1965**, *87*, 2779−2788.
(77) Saenger, W.; Noltemeyer, M.; Manor, P. C.; Hingerty, B.; Klar, B. "Induced-Fit"-Type Complex Formation of the Model Enzyme α-Cyclodextrin. *Bioorg. Chem.* **1976**, *5*, 187−195.
(78) Rong, D.; D'Souza, V. T. A Convenient Method for Functionalization of the 2-Position of Cyclodextrins. *Tetrahedron Lett.* **1990**, *31*, 4275−4278.
(79) Takeo, K.; Ueraura, K.; Mitoh, H. Derivatives Of α-Cyclodextrin and the Synthesis of 6-O-α-D-Glucopyranosyl-α-Cyclodextrin. *J. Carbohydr. Chem.* **1988**, *7*, 293−308.
(80) Takeo, K.; Mitoh, H.; Uemura, K. Selective Chemical Modification of Cyclomalto-oligo-saccharides via Tert-butyldimethylsilylation. *Carbohydr. Res.* **1989**, *187*, 203−221.
(81) Coleman, A. W.; Zhang, P.; Parrot-lopez, H.; Ling, C.-C.; Miocque, M.; Mascrier, L. The First Selective Per-Tosylation of the Secondary OH-2 of β-Cyclodextrin. *Tetrahedron Lett.* **1991**, *23*, 3997−3998.

https://doi.org/10.1021/jacs.3c04111
J. Am. Chem. Soc. 2023, 145, 12894−12910

(82) Ueno, A.; Breslow, R. Selective Sulfonation of a Secondary Hydroxyl Group of β-Cyclodextrin. *Tetrahedron Lett.* **1982**, *23*, 3451−3454.
(83) Fujita, K.; Nagamura, S.; Imoto, T.; Tahara, T.; Koga, T. Regiospecific Sulfonation of Secondary Hydroxyl Groups of α-Cyclodextrin. Its Application to Preparation of 2A2B-, 2A2C-, and 2A2D-Disulfonates. *J. Am. Chem. Soc.* **1985**, *107*, 3233−3235.
(84) Fujita, K.; Nagamura, S.; Imoto, T. Convenient Preparation and Effective Separation of the C-2 and C-3 Tosylates of α-Cyclodextrin. *Tetrahedron Lett.* **1984**, *25*, 5673−5676.
(85) Wang, B.; Zaborova, E.; Guieu, S.; Petrillo, M.; Guitet, M.; Blériot, Y.; Ménand, M.; Zhang, Y.; Sollogoub, M. Site-Selective Hexa-Hetero-Functionalization of α-Cyclodextrin an Archetypical C_6-Symmetric Concave Cycle. *Nat. Commun.* **2014**, *5*, 1−7.
(86) Liu, J.; Wang, B.; Przybylski, C.; Bistri-aslanoff, O.; Ménand, M.; Zhang, Y.; Sollogoub, M. Programmed Synthesis of Hepta-Differentiated β-Cyclodextrin: 1 out of 117655 Arrangements. *Angew. Chem., Int. Ed.* **2021**, *60*, 12090−12096.
(87) Melton, L. D.; Slessor, K. N. Synthesis of Monosubstituted Cyclohexaamyloses. *Carbohydr. Res.* **1971**, *18*, 29−37.
(88) Lai, X.; Ng, S. Convenient Synthesis of Mono (6A-*N*-Allylamino-6 A-Deoxy)-Permethylated β-Cyclodextrin: A Promising Chiral Selector for an HPLC Chiral Stationary Phase. *Tetrahedron Lett.* **2004**, *45*, 4469−4472.
(89) Muderawan, I. W.; Ong, T.; Lee, C.; Young, D. J.; Ching, C. B.; Ng, S. C. A Reliable Synthesis of 2- and 6-Amino-β-Cyclodextrin and Permethylated-b-Cyclodextrin. *Tetrahedron Lett.* **2005**, *46*, 7905−7907.
(90) Tang, W.; Ng, S. C. Facile Synthesis of Mono-6-Amino-6-Deoxy-α-, β-, γ-Cyclodextrin Hydrochlorides for Molecular Recognition, Chiral Separation and Drug Delivery. *Nat. Protoc.* **2008**, *3*, 691−697.
(91) Sakuraba, H.; Maekawa, H. Enantioselective Oxidation of Sulfides Catalyzed by Chiral MoV and Cu^{II} Complexes of Catechol-Appended β-Cyclodextrin Derivatives in Water. *J. Inclusion Phenom. Macrocyclic Chem.* **2006**, *54*, 41−45.
(92) El-Kamel, A. H.; Abdel-Aziz, A. A.; Fatani, A. J.; El-Subbagh, H. I. Oral Colon Targeted Delivery Systems for Treatment of Inflammatory Bowel Diseases : Synthesis, In Vitro and In Vivo Assessment. *Int. J. Pharm.* **2008**, *358*, 248−255.
(93) Rizzarelli, E.; Vecchio, G.; Puglisi, A.; La Mendola, D. Cyclodextrins Functionalised with Etodolac as Specific Site Release Agents, European Patent Office EP1860110B1, 2007.
(94) Wang, H.; Cao, R.; Ke, C.-F.; Liu, Y.; Wada, T.; Inoue, Y. Diastereomeric Molecular Recognition and Binding Behavior of Bile Acids by L/D-Tryptophan-Modified β-Cyclodextrins. *J. Org. Chem.* **2005**, *70*, 8703−8711.
(95) Mcnaughton, M.; Engman, L.; Birmingham, A.; Powis, G.; Cotgreave, I. A. Cyclodextrin-Derived Diorganyl Tellurides as Glutathione Peroxidase Mimics and Inhibitors of Thioredoxin Reductase and Cancer Cell Growth. *J. Med. Chem.* **2004**, *47*, 233−239.
(96) Benesi, H. A.; Hildebrand, J. H. A Spectrophotometric Investigation of the Interaction of Iodine with Aromatic Hydrocarbons. *J. Am. Chem. Soc.* **1949**, *71*, 2703−2707.
(97) Scott, R. L. Some Comments on the Benesi-Hildebrand Equation. *Recl. des Trav. Chim. des Pays-Bas* **1956**, *75*, 787−789.
(98) Scatchard, G. The Attractions of Proteins for Small Molecules and Ions. *Ann. N. Y. Acad. Sci.* **1949**, *51*, 660−672.
(99) Jenie, S. N. A.; Hickey, S. M.; Du, Z.; Sebben, D.; Brooks, D. A.; Voelcker, N. H.; Plush, S. E. A Europium-Based 'off-on' Colourimetric Detector of Singlet Oxygen. *Inorg. Chim. Acta* **2017**, *462*, 236−240.
(100) Wang, J.; Qiu, Z.; Wang, Y.; Li, L.; Guo, X.; Pham, D. T.; Lincoln, S. F.; Prud'homme, R. K. Supramolecular Polymer Assembly in Aqueous Solution Arising from Cyclodextrin Host-Guest Complexation. *Beilstein J. Org. Chem.* **2016**, *12*, 50−72.
(101) Becke, A. D. Density-Functional Thermochemistry. III. The Role of Exact Exchange. *J. Chem. Phys.* **1993**, *98*, 5648−5652.
(102) Lee, C.; Yang, W.; Parr, R. G. Development of the Colic-Salvetti Correlation-Energy Formula into a Functional of the Electron Density. *Phys. Rev. B* **1988**, *37*, 785−789.
(103) Vosko, S. H.; Wilk, L.; Nusair, M. Accurate Spin-Dependent Electron Liquid Correlation Energies for Local Spin Density Calculations: A Critical Analysis. *Can. J. Phys.* **1980**, *58*, 1200−1211.
(104) Stephens, P. J.; Devlin, F. J.; Chabalowski, C. F.; Frisch, M. J. Ab Initio Calculation of Vibrational Absorption and Circular Dichroism Spectra Using Density Functional Force Fields. *J. Phys. Chem.* **1994**, *98*, 11623−11627.
(105) Godbout, N.; Salahub, D. R.; Andzelm, J.; Wimmer, E. Optimization of Gaussian-Type Basis Sets for Local Spin Density Functional Calculations. Part I. Boron through Neon, Optimization Technique and Validation. *Can. J. Chem.* **1992**, *70*, 560−571.
(106) Sosa, C.; Andzelm, J.; Elkin, B. C.; Wimmer, E.; Dobbs, K. D.; Dixon, D. A. A Local Density Functional Study of the Structure and Vibrational Frequencies of Molecular Transition-Metal Compounds. *J. Phys. Chem.* **1992**, *96*, 6630−6636.
(107) Grimme, S. Semiempirical GGA-Type Density Functional Constructed with a Long-Range Dispersion Correction. *J. Comput. Chem.* **2006**, *27*, 1787−1799.
(108) Grimme, S.; Antony, J.; Ehrlich, S.; Krieg, H. A Consistent and Accurate Ab Initio Parametrization of Density Functional Dispersion Correction (DFT-D) for the 94 Elements H-Pu. *J. Chem. Phys.* **2010**, *132*, 154104.
(109) Grimme, S.; Ehrlich, S.; Goerick, L. Effect of the Damping Function in Dispersion Corrected Density Functional Theory. *J. Comput. Chem.* **2011**, *32*, 1457−1465.
(110) Carlqvist, P.; Maseras, F. A Theoretical Analysis of a Classic Example of Supramolecular Catalysis. *Chem. Commun.* **2007**, *7*, 748−750.

https://doi.org/10.1021/jacs.3c04111
J. Am. Chem. Soc. 2023, 145, 12894−12910